

Thermo-kinematic modeling of detachment-dominated extension, northeastern Death Valley area, USA: Implications for mid-crustal thermal-rheological evolution

Brandon M. Lutz^{a,*}, Richard A. Ketcham^b, Gary J. Axen^a, Mengesha A. Beyene^{c,d}, Michael L. Wells^c, Jolante W. van Wijk^a, Daniel F. Stockli^b, Jake I. Ross^e

^a Earth and Environmental Science, New Mexico Institute of Mining and Technology, 801 Leroy Place, Socorro, NM 87801, USA

^b Department of Geological Sciences, Jackson School of Geosciences, University of Texas at Austin, Austin, TX 78712, USA

^c Department of Geoscience, University of Nevada Las Vegas, Las Vegas, NV 89154, USA

^d Turner Fairbank Highway Research Center, Federal Highway Administration, McLean, VA 22101, USA

^e New Mexico Bureau of Geology and Mineral Resources, 801 Leroy Place, Socorro, NM 87801, USA

ARTICLE INFO

Keywords:

Detachment
Metamorphic core complex
Thermo-kinematic model
Mid-crustal flow
Cordilleran thrust belt

ABSTRACT

The deep structure of continental detachment faults remains debated. Thermo-mechanical models generate detachments that either transect the lithosphere or become distributed shear zones in the mid-lower crust, depending on prescribed thermo-rheological conditions. However, these geometries and prescribed conditions remain little constrained by geology-based reconstructions. We present stepwise, balanced reconstructions of a 160 km-long cross-section through two detachment faults in the southwest USA. Reconstructions form the basis of iteratively improved 2D forward thermo-kinematic numerical simulations of detachment fault slip, footwall exhumation, heat advection, and footwall zircon (U-Th)/He cooling ages. Thermo-kinematic model solutions are calibrated iteratively against surface heat flow, pre- and post-extensional geotherms, inferred Moho temperatures, and thermochronometric data from one detachment footwall. Best-fit models predict the thermal and geometric evolution of the crust and detachments, respectively, during extension. The detachment initially rooted into a mid-crustal shear zone (~7.5–12 km depth) and was probably delocalized in the deep middle crust (>12–15 km). The maximum principal stress was likely non-vertical in the middle crust at detachment initiation, possibly due to mantle upwelling. Our reconstructions suggest that the upper crust and lower crust-mantle lithosphere were decoupled by a weak, mid-crustal layer during early detachment faulting. The weak layer was thinned, cooled, partially embrittled, and therefore strengthened by continued detachment slip. This increased lithospheric mechanical coupling and caused the locus of upper-crustal extension to shift. Thinning of a weak mid-crustal layer, as is thought to precede coupled hyperextension and mantle exhumation during rifting, was mostly complete in our study area by ~7–6 Ma.

1. Introduction

Controls on rift system evolution have been explored by geodynamic models, which often aim to replicate certain features identified in seismic reflection profiles of magma-poor rifted margins (e.g. distal, necking, and proximal domains). However, rifted margins only reveal the final result of tens of millions of years of stretching, faulting, hyperextension, mantle exhumation, and breakup. Here, we demonstrate that accurate kinematic reconstructions and forward thermal modeling can inform the changing fault geometries, thermal evolutions, and strain

partitioning of pre-breakup rift phases.

We present regional-scale cross section reconstructions and thermo-kinematic models of detachment faulting and metamorphic core complex (MCC) exhumation in the southwestern USA Cordilleran MCC belt (Fig. 1). Along much of this belt, the crust has been thinned locally from 50 to 60 km (Coney and Harms, 1984; Bahadori et al., 2018; Chapman et al., 2019) to <30 km (Gilbert, 2012). Much of the associated crustal extension was achieved in Oligocene-Miocene times by regional, large-slip detachment faults (e.g. Wernicke, 1992; McQuarrie and Wernicke, 2005). We show stepwise kinematic reconstructions of detachment fault

* Corresponding author.

E-mail address: Lutz.brandon1@gmail.com (Brandon M. Lutz).

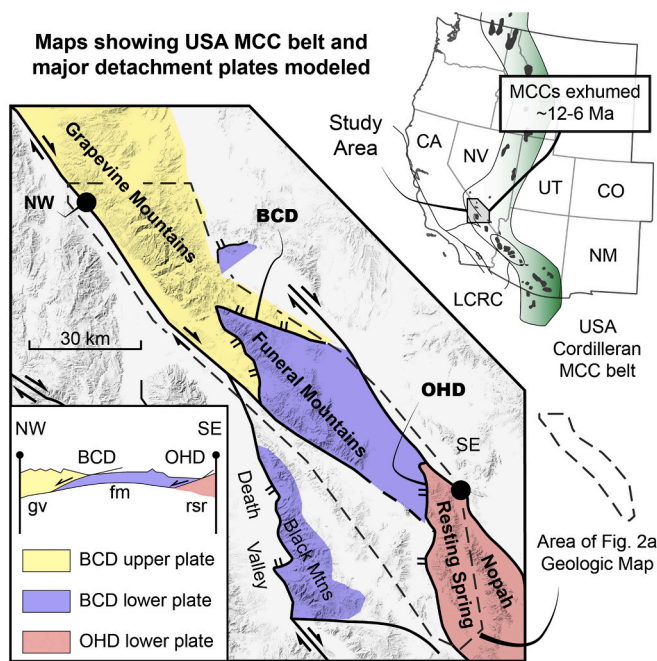


Fig. 1. Map of the western USA showing the generally N-S belt of Cordillera Metamorphic Core Complexes (MCCs) (right) (after Wust, 1986) and map of the central Death Valley region, USA (left), showing major extensional plates modeled in this study. The NW-SE cross-section (bottom left) shows the basic structure of the two detachments modeled in this study. LCRC: Lower Colorado River Corridor.

slip, footwall tilting and exhumation, and basin development related to one of the youngest MCCs in the western US (Fig. 1), which is located in the Eastern California Shear Zone. The kinematic reconstructions are constrained by well-documented structural relations, thermochronology, *syn*-extensional basin histories, and paleo-topography.

Stepwise kinematic reconstructions define a velocity field through time, which is used to simulate crustal area balance and advective heat flow. A horizon line that connects thermochronological sample sites from the Boundary Canyon detachment (BCD; Figs. 1 & 2) footwall is tracked through temperature-time space, and model zircon (U-Th)/He (ZHe) cooling ages are calculated (e.g., Almendral et al., 2015). The evolving detachment geometry and footwall exhumation path are iteratively adjusted until model cooling ages match existing thermochronology (Beyene, 2011), allowing iterative calibration of the cross-sectional reconstruction. Thermo-kinematically-modeled cross-sections have been presented for thrust-related exhumation (Batt and Braun, 1999; Chapman et al., 2017; McQuarrie and Ehlers, 2017; McQuarrie and Ehlers, 2015; Mora et al., 2015; Rak et al., 2017; Yonkee et al., 2019), but extensional thermo-kinematic models have generally been limited to more-idealized scenarios or local reconstructions (Ketchum, 1996; Robinson et al., 2010; Johnstone and Colgan, 2018; Helfrich et al., 2020). Here, cross sections were reconstructed using the Move software (<https://www.petex.com/products/move-suite>), and thermo-kinematic models were created using FETKin (Almendral et al., 2015) and FET-KinPrep (Carrillo et al., 2016).

Our models demonstrate fault geometric, kinematic, and thermal evolutions during the extension/thinning phase of continental rifting. Specifically, we show that the Boundary Canyon detachment (BCD), which accommodated ~35–40 km of extension, did not penetrate the entire crust, but soled into a weak layer that decoupled (or weakly coupled) upper crustal extension from that in the lower crust and mantle lithosphere (e.g., Reston, 1990a/b).

Extension, thinning, and cooling of the weak crustal layer during footwall uplift and exhumation (“occlusion” of Wernicke, 1992,

“annealing” of Pérez-Gussinyé and Reston, 2001) are predicted by our thermal models and crustal area balance. This process likely changed the mechanical architecture of the lithosphere from a decoupled “jelly sandwich” to a thin and weak, but mechanically-coupled “crème brûlée” rheology (Jackson, 2002; Burov and Watts, 2006). Mid-crustal uplift, thinning, and cooling shown by our models facilitates interaction between brittle faults and shear zones in the lower crust and mantle lithosphere (e.g., Pérez-Gussinyé and Reston, 2001; Reston, 2009; Mohn et al., 2012), leading to the transition between relatively distributed extension/thinning to coupled hyperextension and mantle exhumation in magma-poor margins (Lavie and Manatschal, 2006; Péron-Pinvidic and Manatschal, 2009; Péron-Pinvidic et al., 2013; Brune et al., 2014; Naliboff et al., 2017).

Our best-fit models predict also that heat advected with the uplifting detachment footwall creates a high geotherm (~40 °C/km), causing a 4–5 km rise of the brittle-plastic transition (BPT) along the BCD. Heat advection, combined with development of creep-prone clay gouge along the shallow detachment, likely reduced the seismogenic-zone thickness from ~5 km to <1 km. We suggest that the thin seismogenic zone may help explain rare large-magnitude seismicity on active low-angle normal faults (Jackson and White, 1989; Wernicke, 1995; Collettini, 2011; Styron and Hetland, 2014), especially where heat flow is high and/or significant exhumation has already occurred.

2. Geologic background

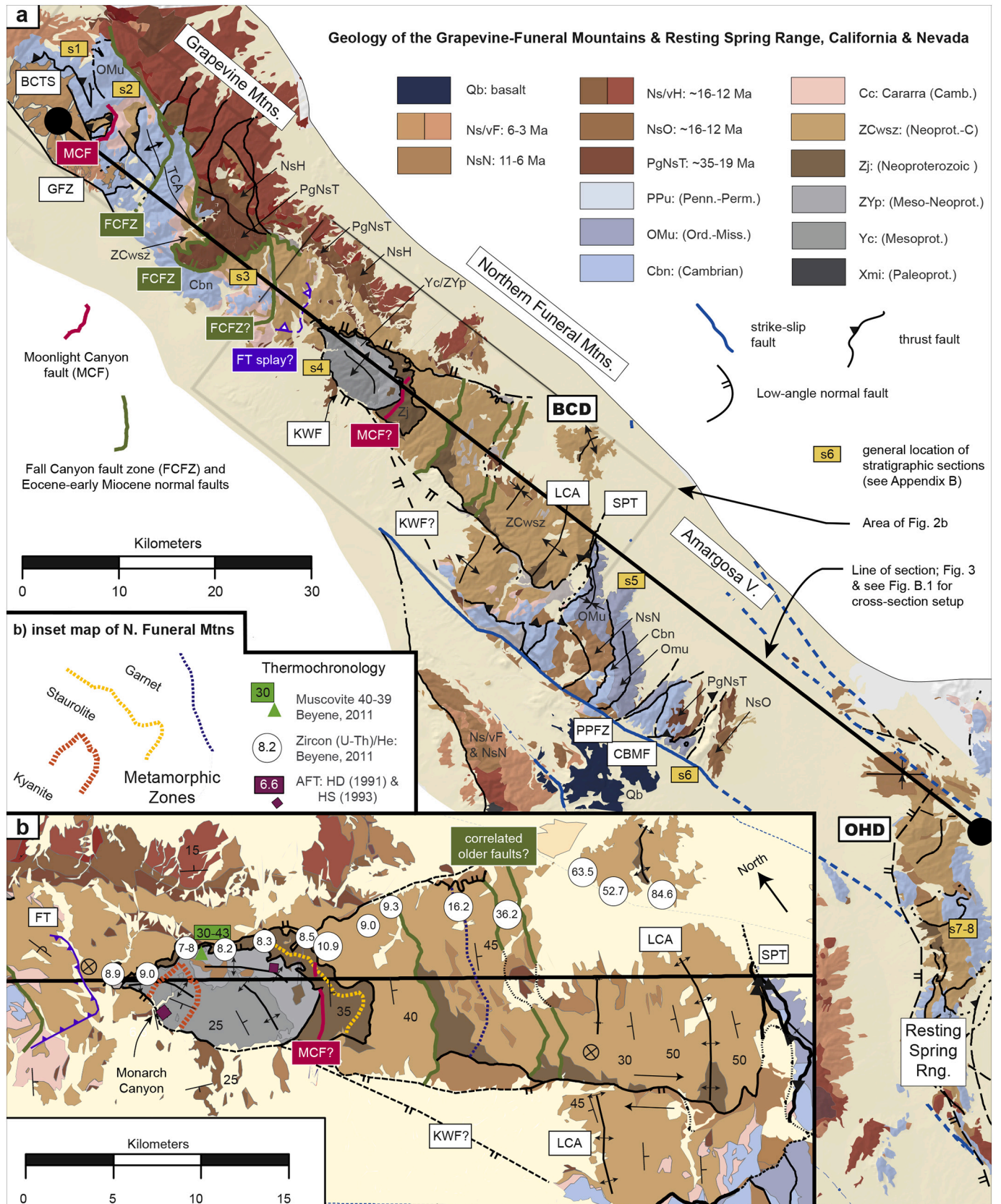
We model a 160-km long, NW-SE cross section through the Grapevine-Funeral Mountains and Nopah-Resting Spring Ranges, northeast of Death Valley (Figs. 1-3 & B.1). The transect demonstrates pervasive extensional dismemberment of the older Cordilleran thrust belt, which likely included local thrust reactivation. The seven thrusts in our cross-section accommodated a total of ~100–125 km of shortening from Late Permian to Cretaceous times (Fig. 3f-h; Appendix A), and normal faults in the cross-section accommodated ~80 km of extension (Fig. 3a-f), primarily in Miocene time (~67 km).

Key geometric, kinematic, and thermal constraints on faults in the model cross section are summarized below (Table 1). We focus on two major detachment faults, but details of both Permo-Mesozoic thrust systems and other Cenozoic normal faults are key to reconstructing the geologic cross-section that forms the basis of our forward thermo-kinematic models (section 3). Supporting details for the modeled thrust geometries are in Appendix A. Our kinematic reconstruction permits revisions to regional thrust plate correlations (Appendix A, Figs. A.3 & A.4), which were used previously to constrain Miocene offsets (e.g., Wernicke et al., 1988; Snow and Wernicke, 2000).

2.1. Detachment faults in the model cross section

The modeled section crosses the Boundary Canyon and Opera House detachment faults (BCD and OHD, respectively), which together accommodated ~70 km of late Miocene, NW-directed upper crustal extension (Fig. 2a & Fig. B.1). The BCD is a low-angle normal fault that juxtaposes Neoproterozoic-Paleozoic sedimentary rocks above amphibolite to sub-greenschist facies metamorphic rocks of the Funeral Mountains MCC (Labotka, 1980; Applegate et al., 1992; Applegate and Hodges, 1995; Hoisch and Simpson, 1993; Mattinson et al., 2007) (Fig. 2b). Lower-plate metamorphic grade decreases monotonically to the SE until footwall sedimentary rocks are reached. Most previous workers estimated 28–40 km of northwest-directed (~300–315°) heave on the BCD (Hoisch and Simpson, 1993; Applegate and Hodges, 1995; Snow and Wernicke, 2000).

Our models incorporate newly recognized offset of older Cenozoic faults and support 35–40 km of BCD slip. Two sets of Eocene-late Miocene normal faults in the northern Funeral Mountains are apparently cut by the BCD (Wright and Troxel, 1993) and are correlated here with similar faults in the Grapevine Mountains (Fig. 2a, Fig. B.1 &



(caption on next page)

Fig. 2. Geologic maps of (a) the study area showing the modeled cross section line (Fig. 3) and (b) the northern Funeral Mountains. s1, s2, etc. mark the locations of type stratigraphic sections used as thicknesses (Appendix B). After compilation of Workman et al. (2016). *Map units:* Qb: Quaternary basalt, Nv/sF: Pliocene sedimentary and volcanic rocks, NsN: late Miocene (~12–7 Ma) sedimentary rocks, NvH: Middle Miocene (~16–12 Ma) volcanic rocks, NsO: Middle Miocene (~16–12 Ma) sedimentary rocks, PgNsT: Middle Eocene-Early Miocene (~40–19 Ma) sedimentary rocks, PPu: Pennsylvanian-Permian sedimentary rocks, OMu: Ordovician-Mississippian sedimentary rocks, Cbn: Cambrian Bonanza King and Nopah Formations, Cc: Cambrian Cararra Formation, ZCwsz: Neoproterozoic-Cambrian Wood Canyon, Stirling, and Zabriskie Formations, ZYp: Meso-Neoproterozoic Pahrump Group, Yc: Mesoproterozoic Crystal Springs Formation, Xmi: basement complex. *Other abbreviations:* AV: Amargosa Valley, BCD: Boundary Canyon detachment, BCTS: Bonnie-Claire thrust system, CBMF: Clery-Bat Mountain fault, FCFZ: Fall Canyon fault zone and other older faults, FT: Funeral thrust splay, GVT: Grapevine thrust, KWF: Keane Wonder fault, LCA: Lee's Camp Anticline, MCF: Moonlight Canyon fault zone, OHD, Opera House detachment, PPFZ: Pyramid Peak fault zone RSR: Resting Spring Range, SPT: Schaub Peak thrust, TCA: Titus Canyon Anticline.

Table 1). The offset normal faults strike approximately perpendicular to the line of section and are shown in the reconstructions (Fig. 3). The east-dipping Moonlight Canyon fault (pink in Figs. 2a, 3, & Fig. B.1) in the Grapevine Mountains (Niemi, 2012) is correlated with a kinematically similar, southeast-dipping normal fault at Monarch Canyon (Fig. 2b & Fig. B.1) in the northwestern Funeral Mountains (Wright and Troxel, 1993) (also pink in Figs. 2a, 3, & Fig. B.1). Southeast of Monarch Canyon ~5 km, northwest-dipping normal faults in the BCD footwall have throws similar to the faults in the Grapevine Mountains (green in Fig. 2). The offset normal faults yield BCD heave of 35–40 km, depending on projections into the cross section (Fig. 2a). We used 37.5 km of heave in our reconstruction and forward models.

Syn-extensional stratal ages and footwall thermochronometry constrain BCD slip to ~12–7 Ma (7.5 mm/yr average slip rate assuming 37.5 km of heave). BCD slip probably initiated just before ~11.5 Ma (age of tuff at base of section), and ended shortly after ~7.5 Ma (age of lava at top of section) (Fridrich and Thompson, 2011; Fridrich et al., 2012). Regression of BCD footwall ZHe ages vs. distance in the slip direction yields an inflection at ~10–11 Ma (Beyene, 2011), interpreted as the initiation of rapid footwall cooling. Beyene's (2011) favored linear regression suggests a slip rate of 8.5 ± 2.0 mm/yr for the BCD, consistent with our prescribed BCD slip rate (7.5 mm/yr). The BCD footwall cooled rapidly (~41 °C/Myr) from ~11–7 Ma, based on combined titanite (9 Ma \pm 2.6 Ma), zircon (10.6 \pm 1.6 Ma), and apatite (6.6 Ma \pm 3 Ma) fission-track ages from Monarch Canyon in the northern Funeral Mountains (Holm and Dokka, 1991). A 5.6 \pm 1.4 Ma apatite fission-track age, collected ~5 km to the southeast of the 6.6 Ma sample (Fig. 2a), records cooling of the BCD footwall (Hoisch and Simpson, 1993) after 7 Ma. We infer that this latest cooling is related to ~4 km of Pliocene-recent exhumation by slip on the NW-SE-trending, range-bounding northern Death Valley and Grapevine fault zones (NDVF & GFZ, respectively; Fig. 2a), which separate northern Death Valley from the Grapevine-Funeral Mountains. These fault zones accommodated at least 5 km of throw, based on gravity data and escarpment height (Blakely et al., 1999), most likely after ca. 7.5–6.5 Ma (Fridrich and Thompson, 2011; Fridrich et al., 2012).

Net slip of the OHD is poorly defined, but syn-orogenic strata and previous reconstructions suggest >25 km of slip from ~16–7 Ma. Southeast-thickening growth strata and anticlinal rollover in the upper plate suggest extension above a listric fault (Cemen et al., 1985; Cemen and Wright, 1990). Gravity-based depth-to-bedrock models indicate an ~3 km thickness of the upper-plate Amargosa Valley basin (Fig. 3a) (Blakely et al., 1999), which is inferred to be filled with both ca. 16–12 Ma and 12–6 Ma packages of synorogenic strata (Cemen et al., 1999; Fridrich et al., 2012) (Fig. 3a–e). Dips in the older package increase northward from 35° to 45° over an ~2 km distance (Fridrich et al., 2012). The area between the Clery thrust in the southeastern Funeral Mountains and the Chicago Pass thrust in the Nopah-Resting Spring Range was extended by at least 200% (Wernicke et al., 1982; Snow and Wernicke, 2000), which supports >18 km of heave on the OHD. Our reconstructions show 22.6 km of heave on the OHD, which includes ~6.9 km of heave on synthetic, upper-plate normal faults in Amargosa Valley and in the Funeral Mountains range block (Table 1 & Fig. 3).

3. Thermo-kinematic model setup

In this section we describe how the geologic cross-section was constructed, retro-deformed to its pre-extension state, and forward modeled (sections 3.1–3.3). Thermo-kinematic finite-element numerical simulations, including constraints on parameter inputs and the results of parameter tests, are described in section 3.4.

3.1. Initial cross-section construction

The structural cross section (Fig. 3 & Fig. B.1) was drafted using standard methods and runs through abundant exposures of bedrock. It runs generally parallel to the regional extension direction (Wernicke et al., 1988; Snow and Wernicke, 2000; McQuarrie and Wernicke, 2005), so standard section balancing methods can be applied (Chamberlain, 1910; Dahlstrom, 1969; Suppe, 1985; Groshong, 1994, 1996; Groshong Jr et al., 2012). The model cross section has 306° azimuth (Figs. 1 & 2a), within the range of BCD upper-plate transport directions determined by previous studies (Table 1). The OHD transport direction is less well-constrained by fault kinematic data, but previous workers interpreted a generally west-northwest-oriented regional extension from fault attitudes and hanging-wall rollover (e.g. Wernicke et al., 1982, 1988; Fridrich et al., 2012). The section also is subparallel to the transport direction of most thrusts in the model transect (generally SE; Fridrich et al., 2012; Table 1), providing an opportunity to examine the superimposed strain patterns.

Faults and unit contacts were projected into the subsurface using surface data, gravity models, and previous cross sections. Shallow (0–2 km depth) fault geometries were generally adapted from previous cross-sections (see Fig. B.1 for adaptations of previous work), though we omitted some small offset (<1 km) faults, combined closely-spaced (1–2 km) faults, and extended fault interpretations deeper to a basal detachment in the basement complex (unit Xmi). The salient aspects of fault geometries and kinematics are given in Table 1. Thermochronometric and structural orientation data within 0–4.5 km of section lines were projected to the sections (Fig. 2b). Thicknesses from published sections (Fig. 3 & Fig. B.2) were used to build the stratigraphy into the subsurface to intersections with projected faults. Normal faults had initially listric geometries, soling into a basal decollement in the regional basement complex (unit Xmi). Fault geometries were modified iteratively to maintain area balance and satisfy thermochronometric constraints on forward thermal models (Fig. 4) (see section 3.2 below).

3.2. Reconstruction and forward kinematic modeling methods

Cross section reconstruction of normal faults and fault-bounded basins was done in several increments, each of which include multiple steps done iteratively (Fig. 4): 1) rigid translation of upper plates, 2) inclined antithetic simple shear to translate upper plate features onto fault footwalls, 3) isostatic adjustments to place detachment footwalls at proper paleo-depths and honor other constraints.

Normal fault hanging walls were first translated as rigid blocks (Fig. 4a/b). Extensional area (Fig. 4b) was calculated based on the prescribed horizontal block motion from offset features and fault

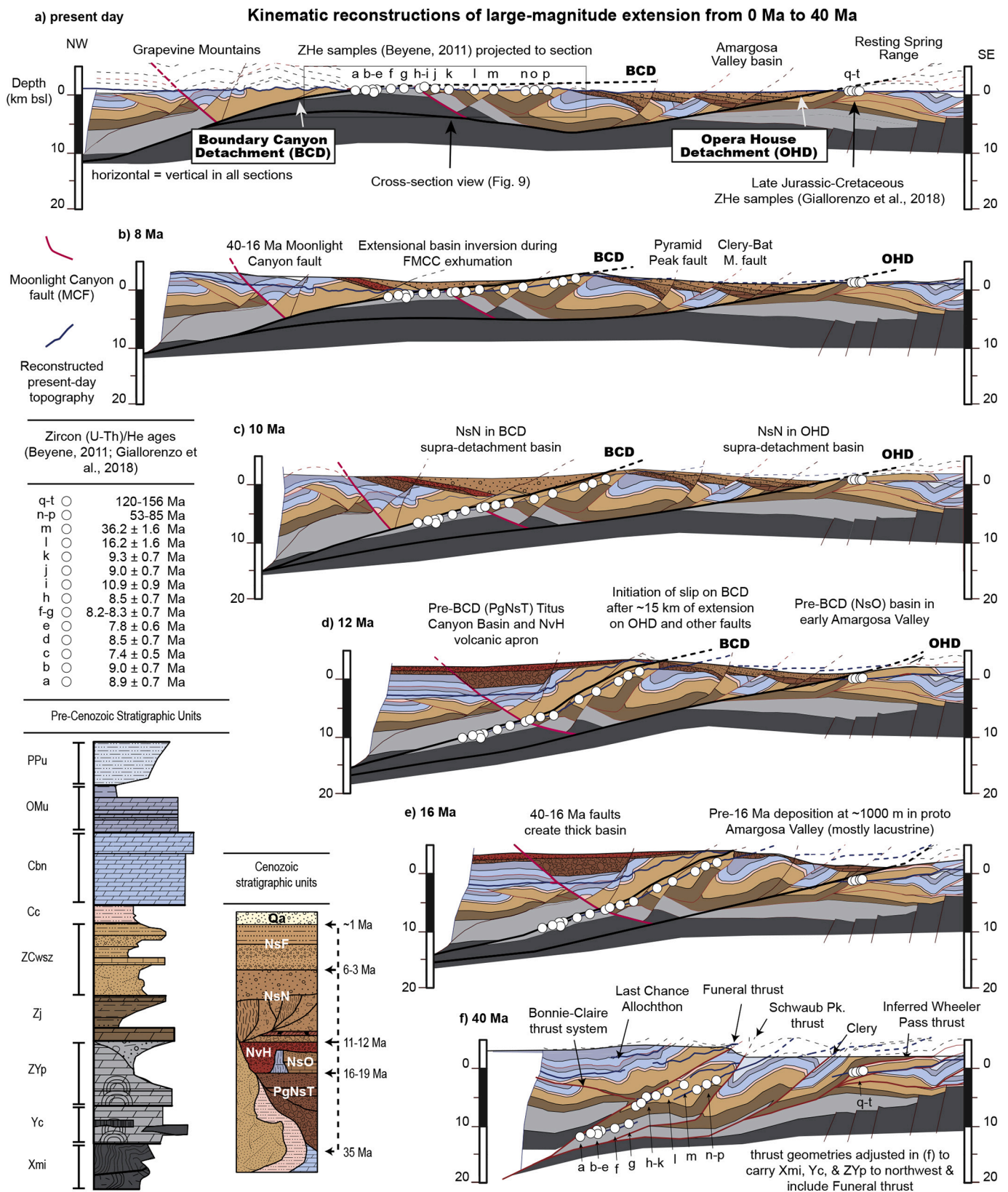


Fig. 3. Snapshots of cross-section reconstructions. a) present-day structural cross section. The section line is shown in Fig. 2a (also see Fig. B.1 for detail). White circles are ZHe sample locations from Beyene (2011; a-p) and Giallorenzo et al. (2018; q-t). b) 8 Ma. c) 10 Ma. d) 12 Ma reconstruction showing all BCD heave restored. e) 16 Ma reconstruction showing all OHD and BCD slip restored. f) ca. 40 Ma reconstruction showing 40–16 Ma extension restored and the basal Cenozoic unconformity (topography line at top of section). g) Late Jurassic-Cretaceous reconstruction showing preferred thrust geometries and approximate burial depths of the FMCC (Appendix A for details). h) Permian reconstruction showing post-Permian thrusts within the model cross-section restored (the Last Chance thrust, some Permian pre-thrust folds, and eastern thrusts off the model cross section remain). Appendix B shows the 16–7 Ma interval in 1-Myr steps.

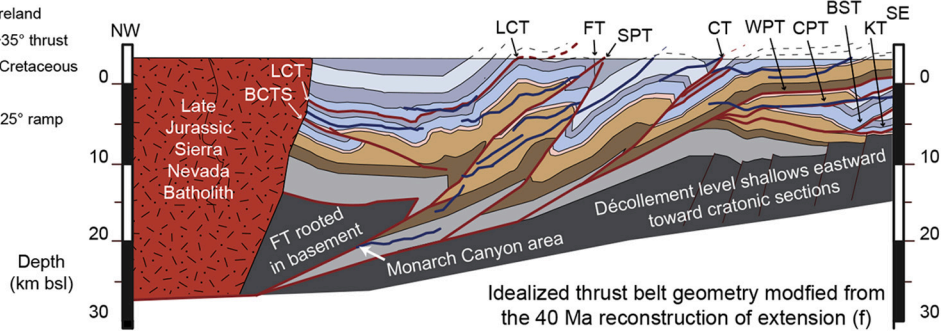
Key notes on thrust belt reconstruction

- 50-55 km shortening along section; 82-98 km including foreland
- Funeral thrust: 12 km max throw, 16 km max shortening ~35° thrust
 - Places Monarch Canyon at ~24 km depth in Jurassic-Cretaceous
 - Suggests non-lithostatic pressure 9-10 kbar
- Wheeler Pass: 7.5 km throw, 20.5 km shortening 15° flat, 25° ramp

Abbreviations:

- LCT: Last Chance thrust
 BCTS: Bonnie Claire thrust system
 FT: Funeral thrust
 SPT: Schaub Peak thrust
 CT: Clery thrust
 WPT: Wheeler Pass thrust
 KT: Keystone thrust
 BST: Baxter-Shaw thrust
 CPT: Chicago Pass thrust

g) Late Jurassic-Cretaceous reconstruction of the Cordilleran thrust belt



h) Late Permian reconstruction of most thrusting in the model transect

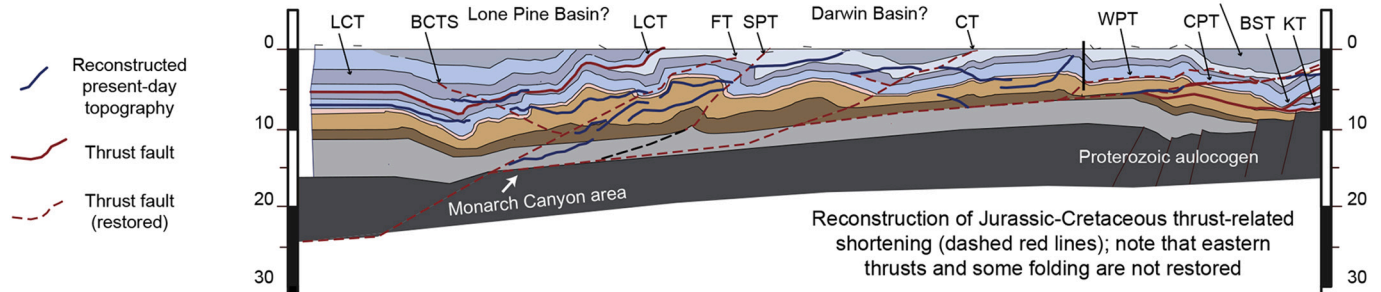


Fig. 3. (continued).

Table 1

Summary of kinematic data and supporting evidence for faults in the modeled cross-section.

Structures	Fault name (abbrev)	Age	Magnitude	Sense	Supporting details
Normal faults	Grapevine fault zone (GFZ)	Pliocene-recent	~5 km T	normal; down-W	4 km deep basin in HW from gravity studies ^a ; cross-cuts Pliocene ^b ; For 7-0 Ma, modeled FW uplift and 0 and 1.5 km net erosion, linearly accrued (0-0.21 mm/yr) (see Fig. 3)
	Boundary Canyon detachment (BCD)	Late Miocene	37.5 km H	top NW; ~312 + - 12	syn-kinematic qtz- and calc-mylonites ^{c,d,e,f} ; cataclases/breccia; foliated gouge; 2-3 km-thick ca. 11.45-7.4 Ma upper plate basin & tectonic mélange ^g
	Pyramid Peak fault system (PPFS)	Miocene	2.5 km H	Oblique-normal; down-NW	rock avalanche breccia ^g ; cuts 40-16 Ma strata, fanning 16-7 Ma stratal dips in HW ^g ; slip calculated from Paleozoic units and projected fault reactivated thrust ^h ; cuts 40-16 Ma strata, fanning 16-7 Ma stratal dips in HW ^g ; slip calculated from Paleozoic units and projected fault fanning dips and ca. 16-7 Ma growth strata in upper plate ^g heave inferred from balanced section; 2-3 km-thick upper plate basin deposited at 1000 ± 500 m elevation ¹ (16-12 Ma) ^g
	Clery-Bat Mountain fault (CBMF)	Miocene	2.7 km H	Normal down-NW	
	Opera House detachment (OHD)	Miocene	29.5 km H	normal; down-NW	
	Fall Canyon fault zone (FCFZ)	Eocene-Miocene	2-2.5 km T	oblique-normal; down-E	Low-angle faults E and W-dipping ¹ ; mostly buttress unconformity with post-16 Ma volcanic rocks ¹ ; some oblique-slip and strike-slip reactivation with little separation of post-13 Ma rocks ¹ ; little to no topographic signature and appears internal to the Grapevine Mountains range block ^b
	Moonlight Canyon fault zone (MCF)	Eocene-Miocene	1.5-2.2 km T;	normal; down-E/W	
	"older faults" in the Funeral M.	Eocene-Miocene	0.5-1.5 km T;	normal-down E/W	
	Wheeler Pass thrust (WPT)	Late Jurassic-Cretaceous (?)	5.9 km ST	ESE	HW syncline; HW flat; FW syncline; Proterozoic on Pennsylvanian-Permian ^k ; inferred beneath Amargosa Valley ^{}
	Chicago Pass thrust (CPT)	Cretaceous (?)	~5 km ST	ESE	HW ramp, FW syncline; Cambrian on Mississippian ^l
Thrusts	Baxter-Shaw thrust	Cretaceous (?)	~4 km ST	ESE	HW ramp-flat, FW syncline frontal imbrication of CPT ^{l, m}
	Clery thrust (CT)	Late Jurassic-Cretaceous (?)	2.5-3 km T	ESE	FW syncline and minor duplex ^h ; Cambrian on Ordovician
	Schaub Peak thrust (SPT)	Late Jurassic-Cretaceous (?)	3.8 km ST	ESE	OT FW syncline and minor duplex; OT HW anticline ^d
	Funeral thrust (FT)	Late Jurassic	5-6 km T	ESE	OT bedding juxtaposed to flat bedding in ZCwsz ⁿ ; required for deep burial in N. Funeral Mtns ^{o,p,*}
	Bonnie-Claire Thrust System (BCTS)	Cretaceous (?)	2.5-3 km ST	WNW	FW imbricated; Cambrian on Mississippian; repeated Ordovician section ^b
	Grapevine Thrust (GVT)	Permian	2.5-5 km ST	ENE	Proterozoic on Mississippian; refolded twice ^b

H: heave; T: throw; ST: stratigraphic throw; HW: hanging wall; FW: footwall; OT: overturned.

**see Appendix for more information.

^aBlakley et al. (1999). ^bNiemi (2012). ^cHoisch and Simpson (1993). ^dWright and Troxel (1993). ^eApplegate and Hodges (1995). ^fBeyene (2011). ^gFridrich et al. (2012). ^hCemen and Wright (1990). ⁱLechler et al. (2013). ^jReynolds (1974). ^kBurchfiel et al. (1974). ^lBurchfiel et al. (1983). ^mPavlis et al. (2014). ⁿWorkman et al. (2016). ^oCraddock-Affinati et al. (2020). ^pHoisch et al. (2014).

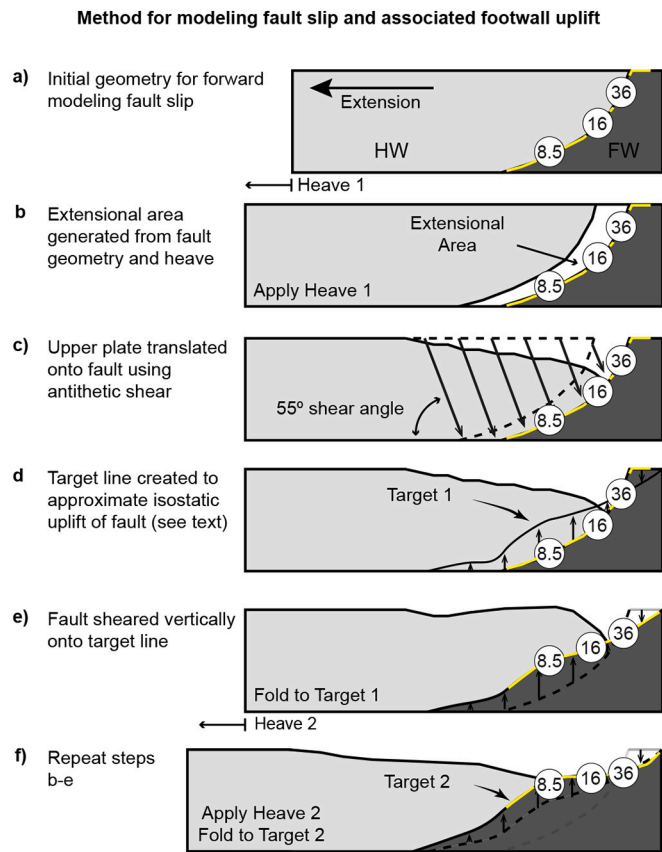


Fig. 4. Inclined, simple-shear, area-balancing method for reconstructing and forward modeling fault displacements, simulating uplift of the detachments, and tracking a “samples” horizon (yellow line) between time-steps. a) initial fault geometry, showing hanging wall and footwall, magnitude of first increment of heave, and thermochronometer sample sites (white circles). b) Heave is applied to rigid upper plate and extensional area is calculated based on heave magnitude and fault geometry (e.g. [Groshong, 1994](#)). c) Upper plate horizons are translated onto the fault plane using simple shear (55° antithetic shear angle). d) A target line is created to simulate the uplifting footwall. Target surfaces were generated such that paleo-elevation and syn-extensional basin thicknesses both honor geological constraints and approximate thermochronometer depths. e) The initial fault and surrounding horizons are translated vertically onto the target line (new detachment). f) The next increment of heave is applied, and steps a-e are repeated. (For interpretation of the references to colour in this figure legend, the reader is referred to the web version of this article.)

geometry ([Groshong, 1994](#)). Hanging-wall formation tops were then translated onto the underlying fault along simple shear planes dipping 55° and spaced 50 m apart horizontally ([Fig. 4c](#)). This shear angle (55°) is approximately the average orientation of antithetic normal faults above the OHD ([Fridrich et al., 2012](#)), and 55° is also convention if the shear angle is poorly constrained. This simple-shear, area-balance method creates anticlinal rollover above listric normal faults.

Changing detachment fault dip during footwall unroofing was simulated by folding the detachment (in forward simulation; unfolding in reconstruction) to a series of target lines using vertical simple shear ([Fig. 4d-f](#)) (e.g. [Wernicke and Axen, 1988](#)). The target lines were hand-drafted and iteratively adjusted, honoring available constraints. Specifically, each of 5 BCD-slip reconstruction steps (37.5 km of heave in 7.5 km increments) required iteratively defining a best-fit target line that 1) kept upper-plate paleoelevation within 1500–2500 m ([Bahadori et al., 2018](#); [Zhou and Liu, 2019](#)) 2) maintained an upper-plate basin thickness of 0–2 km at 500–1500 m paleoelevation (e.g. [Lechler et al., 2013](#); [Fridrich and Thompson, 2011](#)), and 3) placed lower plate ZHe

thermochronometric sample locations ([Beyene, 2011](#)) at reasonable paleo-depths. Multiple target lines were tested, and target lines were iteratively adjusted after forward thermo-kinematic modeling to find the best fit to the thermochronometric data (section 3.4). We use subvertical simple shear (e.g., [Wernicke and Axen, 1988](#)) to simulate incremental detachment footwall uplift, rather than flexural isostatic approaches ([Buck, 1988](#); [Long and Walker, 2015](#)) that require very small effective elastic thicknesses (<2 km) to simulate footwall exhumation and cooling rates consistent with thermochronometry and tilt-reconstructions.

3.3. Kinematic reconstructions and fault slip rates

Using the above iterative method, a series of structural reconstructions were made from present to Eocene ([Fig. 3a-f](#)). The reconstructions were created by portioning heave values for individual faults into their time intervals of activity ([Table 2](#)). These reconstructions form the basis of the iterative thermo-kinematic model time-steps ([Fig. 3a-f](#) & [Appendix B](#)), in which tracked horizons were converted to average interval velocities ([Carrillo et al., 2016](#)) ([Figs. 5 & 6](#)). The Jurassic and Permo-Triassic reconstructions ([Fig. 3f/g](#)) were not thermo-kinematically modeled.

3.4. Thermo-kinematic modeling

The kinematic model is transformed into a thermo-kinematic model using FETKinPrep ([Carrillo et al., 2016](#)) and FETKin ([Almendral et al., 2015](#)). FETKinPrep tracks formation tops between reconstruction time-steps and converts their displacements to motion vectors ([Figs. 5-7](#)). Whereas velocities for the upper 10 km of the numerical model domain are well-constrained by horizon-tracking between kinematic time-steps ([Figs. 3 & 4](#)), velocities in the middle part of the model domain are uncertain, and were therefore generated using three mid-crustal area-balancing schemes ([Figs. 6 & 7](#)). These are similar to those presented in [Ketcham \(1996\)](#), but linked directly to the kinematic-model-derived uplift ([Carrillo et al., 2016](#)) rather than an arbitrary, user-entered function.

We tested three different methods for balancing mid-lower crustal uplift with prescribed upper crustal extension ([Table 2](#)). The first is a “uniform stretching” model for the middle crust ([Fig. 6a/b](#)), in which area balance is achieved by laterally homogeneous thinning of the middle crust to account for the extensional area (yellow in [Fig. 6a](#)) prescribed by kinematic reconstructions (grey arrows in [Fig. 6b](#)). Mid-crustal vectors (blue arrows in [Fig. 6b](#)) are then generated to simulate the evenly distributed thinning. In the second “stacked” scheme ([Fig. 6c/d](#)), mid-crustal uplift and thinning vary laterally and are weighted in direct proportion to upper-crustal exhumation prescribed in kinematic reconstructions ([Figs. 6c/d & 4d-f](#)), producing a “stacked” pattern, in which mid-crustal uplift is concentrated beneath areas of upper crustal thinning. The stacked method simulates extreme necking of the crust beneath the uplifting detachment footwall.

The third (and preferred) method is an inverse-weighted uplift scheme, where upper-crustal extension is balanced by thinning of the middle crust laterally away from areas of concentrated upper crustal exhumation ([Ketcham, 1996](#)) ([Fig. 6e/f](#)). In this method, the middle crust thins most in regions laterally removed from areas of concentrated upper crustal thinning, leaving the area beneath the MCC relatively thicker. This approach roughly simulates isostatic compensation by mid- to lower crustal flow and distributes basal uplift, consistent with little Moho depth variation across the model cross-section ([Gilbert, 2012](#)) ([Fig. 7](#)).

Mid-crustal balancing is approximated by defining advection vectors within a region bounded by two depths at the beginning of a time step that maintain area balance of that layer through the end of the step, compensating for lengthening by thinning. We call the upper boundary the compensation depth, as its uplift is a direct function of overlying thinning or thickening, and the lower boundary is called the upwelling

Table 2
Kinematic inputs for stepwise fault reconstructions and forward models.

Fault	Interval (Ma)	Heave (km)	Rate (mm/yr)
Moonlight Canyon fault zone	40–16	4.0	0.2
Fall Canyon fault zone1	40–16	4.0	0.2
Fall Canyon fault zone2	40–16	4.0	0.2
subtotal	40–16	12.0	0.5
OHD1	16–7	22.6	2.5
OHD2	16–7	6.9	0.8
CBMF	16–7	2.7	0.3
PPFS	16–7	2.5	0.3
Subtotal	16–12	15.4	3.9
Subtotal	16–7	34.7	3.9
BCD	12–7	37.5	7.5
Total	40–7	84.2	2.6
Total	16–7	72.2	8.0
Total	12–7	56.8	11.4

Supporting details for intervals and magnitudes in text and Table 1.

depth. Below the upwelling depth, the crust is assumed to spread or flow uniformly. We tested various upwelling and compensation depths for the mid-crustal area balance (Table 3). In preferred tests, we used upwelling and compensation depths of 20 km and 10 km, respectively (Fig. 7) in order to control the heat advection associated with mid-crustal uplift, which was too high in tests with deeper upwelling (Table 3). The shallow compensation depth yielded the best fits to multiple validity criteria, which are detailed below. We note that the compensation depth is not the same as isostatic compensation depth referred to in flexural or local isostasy studies, but instead the upper boundary of the mid-crustal area that is being balanced.

Once the velocity field is defined by horizon tracking and mid-crustal area balance, FETKin then solves the heat flow equation on a 2D Lagrangian finite-element grid:

$$\rho c \left[(\delta T / \delta t) - v_x (\delta T / \delta x) - v_y (\delta T / \delta y) \right] = (\delta / \delta x) k (\delta T / \delta x) + (\delta / \delta y) k (\delta T / \delta y) + \rho H$$

where ρ is rock density (kg m^{-3}), c is heat capacity ($\text{J kg}^{-1} \text{K}^{-1}$), T is temperature (K), t is time (s). v_x and v_y are the horizontal and vertical components of the velocity field, respectively, k is thermal conductivity ($\text{W m}^{-1} \text{K}^{-1}$), and H is heat generation (W m^{-3}).

Our numerical model domain is 160 km horizontally by 30 km vertically (Fig. 5) with prescribed upper (Earth surface) and lower boundary conditions. The upper boundary conditions are given by

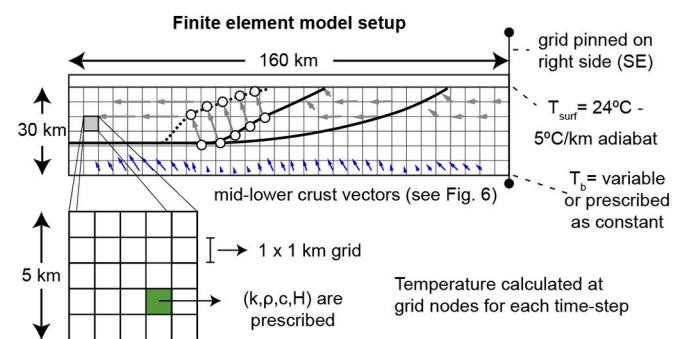


Fig. 5. FETKin finite-element schematic setup showing model domain, grid size, velocity vectors, and boundary conditions. The samples horizon (dashed black line with white dots) is uplifted and eventually brought to the surface in forward models. Stepwise reconstructions of Fig. 3 define the upper crustal velocity field (grey arrows), which is broken into x- and y- components to calculate advective heat transport. Mid-lower crustal vectors (blue arrows) are generated from the area-balancing scheme shown in Fig. 6. See text for discussion. (For interpretation of the references to colour in this figure legend, the reader is referred to the web version of this article.)

Almendral et al. (2015):

$$T [t, x, y = S(x)] = T_s(y) = T_{\text{MSL}} + \beta [y - y_{\text{max}}]$$

where $S(x)$ is the topography line prescribed by the kinematic reconstructions, T_{MSL} is temperature at mean sea level (24°C), $T_s(y)$ is the top surface temperature, β is the lapse rate (-5°C/km), and y_{max} is the mean sea level.

Heat flux is zero at the right- and left-hand sides of the model domain:

$$[\delta T / \delta x] = 0$$

We tested two different types of basal thermal boundary conditions: constant basal temperature ($T_{\text{basal}} = 800^\circ\text{C}$), or constant basal thermal gradient ($[\delta T / \delta z]_{\text{basal}} = 20\text{--}30^\circ\text{C/km}$).

$$T [x, y = y_{\text{min}}] = T_{\text{basal}}$$

$$[\delta T / \delta z]_{\text{basal}} = 20 - 30^\circ\text{C km}^{-1}$$

where y_{min} is the model's base level. The constant basal gradient condition allows temperature to change in response to processes affecting heat flow within the grid (e.g. exhumation of deep/hot rocks, lateral topographic gradients). The initial condition is calculated as the steady state temperature distribution based on the boundary conditions used.

Our preferred thermal properties were adapted from measurements made on the regional Mojave Province basement complex (unit Xmi). These are thermal conductivity, $k = 2.51 \text{ W m}^{-1} \text{ K}^{-1}$; density, $\rho = 2800 \text{ kg m}^{-3}$; heat capacity, $c = 1100 \text{ J kg}^{-1} \text{ K}^{-1}$; and heat production, $H = 0.4\text{--}1.4 \mu\text{W m}^{-3}$ (Sass et al., 2008), fairly consistent with global average values of granitic gneiss and amphibolite gneiss (Pinet and Jaupart, 1987; Eppelbaum et al., 2014; Jaupart et al., 2016). Model sensitivity to varying material thermal properties (k , ρ , c , H) was tested (Table 3 & Appendix D). Modern heat flow ($75\text{--}90 \text{ mW m}^{-2}$; Blackwell et al., 2011) and late Miocene shallow geothermal gradients ($\sim 25\text{--}35^\circ\text{C/km}$) fit better with lower heat production tests ($0.4 \mu\text{W m}^{-3}$) (Table 3).

Model cooling histories and cooling ages are generated in FETKin by tracking the temperature-time history of a "samples horizon" (Figs. 4 & 5), which connects the locations of actual ZHe samples from the BCD footwall (Beyene, 2011; Figs. 2b & 3a). Model sample cooling ages are then calculated using standard diffusion kinetics for the ZHe system (Reiners, 2005). Model cooling ages were compared to actual cooling ages from Beyene (2011) (Figs. 2b & 3), and the geometric initial condition and kinematic-thermal modeling were repeated until model cooling ages matched the actual data.

3.5. Validity of thermal model solutions

The validity of thermo-kinematic models was evaluated through parameter testing (Table 3 & Appendix D) and comparison of temperature solutions to interpolated heat flow, nearby measured heat flow, regional pre- and post-extensional geothermal gradient, and Moho temperature benchmarks. We determined that acceptable models should 1) predict 0 Ma surface heat flow ranging from 75 to 90 mW m^{-2} , with slightly higher values to the northwest (Blackwell et al., 2011), 2) yield pre- and post-extensional geothermal gradients of $15\text{--}31^\circ\text{C/km}$ and $25\text{--}40^\circ\text{C/km}$, respectively, consistent with tilting reconstructions and HeFTy models from nearby normal fault footwalls (Holm et al., 1992; Stockli et al., 2003; Fitzgerald et al., 2009; Blackwell et al., 2011; Bidgoli et al., 2015a/b), 3) predict present-day temperatures of $800\text{--}850^\circ\text{C}$ at $30 \pm 7 \text{ km}$ depth (Gilbert, 2012; Schutt et al., 2018), and 4) match the BCD footwall cooling history as recorded by thermochronological samples (Holm and Dokka, 1991; Hoisch and Simpson, 1993; Beyene, 2011).

We target 0 Ma basal model temperatures of $800\text{--}900^\circ\text{C}$ ($\sim 24\text{--}31 \text{ km}$ depth), based on Moho temperature estimated from mantle P-wave velocities ($800\text{--}850 \pm 50^\circ\text{C}$ at depth of $30 \pm 7 \text{ km}$) (Gilbert,

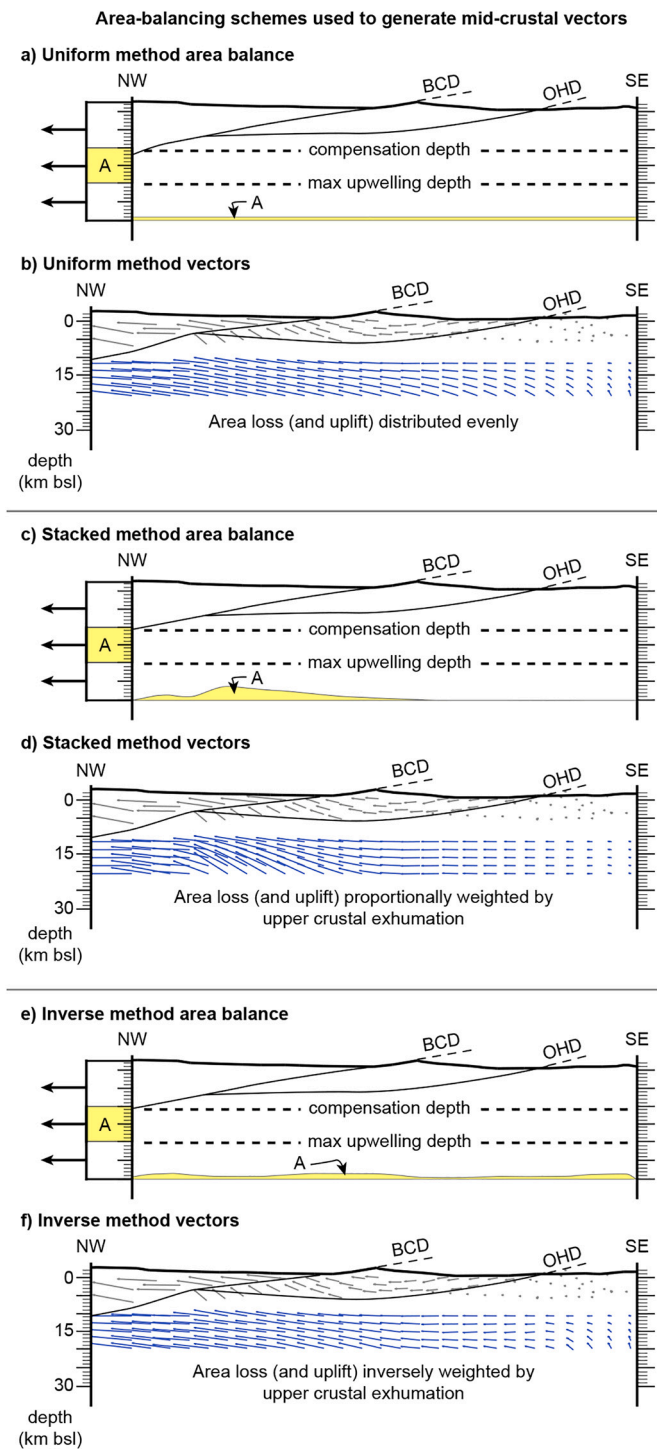


Fig. 6. 2D cross-sections of the model grid showing the three separate area-balancing schemes used to model mid-crustal velocities (blue arrows): uniform (a-b), stacked (c-d), and inverse (e-f). Extensional area (A) is calculated from the mid-crustal component of extension, below where the upper crust is balanced by the kinematic model (grey arrows from reconstruction). This extensional area (A) is balanced by basal uplift from a prescribed depth of upwelling (e.g. 20–30 km; Table 3). The laterally-varying magnitude of mid-crustal uplift needed to compensate the extensional area (A) depends on the balancing method used. See text for more discussion. (For interpretation of the references to colour in this figure legend, the reader is referred to the web version of this article.)

2012; Schutt et al., 2018). Models run with constant basal temperature of 800 °C honor this condition well (e.g. ZHe_{800 g}; Table 3; Figs. 7 & 8). Models run with a basal gradient of 22.5 °C/km predict reasonable 0 Ma basal temperatures, depending on area-balancing scheme (Table 3 & Fig. 7). We prefer the inverse area balance method, which minimizes heat advection beneath the detachment footwall, because it yields smoother 0 Ma basal temperatures that are consistent with Schutt et al. (2018) and less implied upwelling of the Moho beneath the MCC (Ketchum, 1996) (Figs. 7 & 8). Of the constant basal gradient tests, the inverse configuration (Fig. 6e/f) yielded the most reasonable basal temperatures while honoring other validity criteria. Models run with basal gradients >22.5 °C/km or those using the stacked method (Figs. 7 & 8) yield modern (0 Ma) basal temperatures up to 1100–1300 °C (Table 3), which are too hot (Schutt et al., 2018).

The statistical similarity between modeled (this study) and actual (Beyene, 2011) sample ages was calculated by a residual sum of squares (RSS) (Table 3). First, both modeled and actual (Beyene, 2011) cooling ages from the BCD footwall were plotted by x-distance along the modeled cross section (in the BCD footwall; Fig. 9). Best-fit 3rd order polynomials were fit to the cooling age vs. x-distance data (see Appendix D & section 4.2). For each parameter test, the RSS was then calculated by squaring the difference between modeled and actual (Beyene, 2011) cooling ages for every x-location. The closer RSS is to zero, the more similar the model is to the Beyene (2011) data. Plots of cooling age vs. distance along the BCD footwall for all parameter tests can be found in Appendix D.

4. Thermo-kinematic model results

Our preferred, best-fit thermo-kinematic models are 1) ZHe_{grad22.5 h} and 2) ZHe_{800 g} (Fig. 9 & Table 3). Of all parameter tests, model ZHe_{grad22.5 h} produces the best fit to the BCD footwall ZHe cooling ages (Beyene, 2011) while satisfying other conditions described above, with some caveats. The ZHe_{grad22.5 h} test yielded a pre-detachment geotherm (16 Ma) of 24–26 °C/km, a post-extensional (0 Ma) shallow geotherm of 31–40 °C/km, and a 0 Ma basal temperature of 900–1000 °C (Fig. 7 & Table 3). The high near-surface geotherm in the northwestern part of the model (northwestern Funeral Mountains and Grapevine Mountains) is reconciled with 75–90 mWm⁻² surface heat flow by treating the surface as low-conductivity (~2.0 W m⁻¹ K⁻¹), due to the predominance of carbonate outcrops there (Fridrich et al., 2012). This low thermal conductivity, however, would not properly treat the entire 160 × 30 km model domain, for which we used 2.5 W m⁻¹ K⁻¹ in preferred models, consistent with both measured and average values for the granitic basement. While the 0 Ma-predicted basal (30 km depth) temperature is slightly higher than that estimated from mantle P-waves (Schutt et al., 2018), the ±7 km uncertainty in crustal thickness estimates (Gilbert, 2012) permits that the Moho could be as shallow as 23 km, where ZHe_{grad22.5 h} predicts temperatures of 800 ± 50 °C consistent with Schutt et al. (2018). The Moho temperature (Schutt et al., 2018) and/or crustal thickness (Gilbert, 2012) models may not capture local variations in modern heat-flow along the model transect (Blackwell et al., 2011). Models ZHe_{grad22.5e} & ZHe_{grad22.5i} yield very good fits to the cooling ages and other validity criteria (Table 3), however they are less-preferred than ZHe_{grad22.5 h} due to the basal temperature criteria (Figs. 7 & 8).

Snapshots of our most-preferred model (ZHe_{grad22.5 h}) (Fig. 10) show the thermal evolution during progressive extension. Here, the temperature-time-depth evolution of modeled and actual samples from the BCD footwall can be visualized. The modeled cooling history of samples for ZHe_{grad22.5 h} is shown in Fig. 11.

4.1. Model cooling rates

In our forward models of exhumation, the BCD footwall undergoes a multi-stage non-linear cooling history (Fig. 11). Maximum model

Thermo-kinematic model snapshots from 12-0 Ma showing the effect of mid-crustal balancing scheme on heat advection

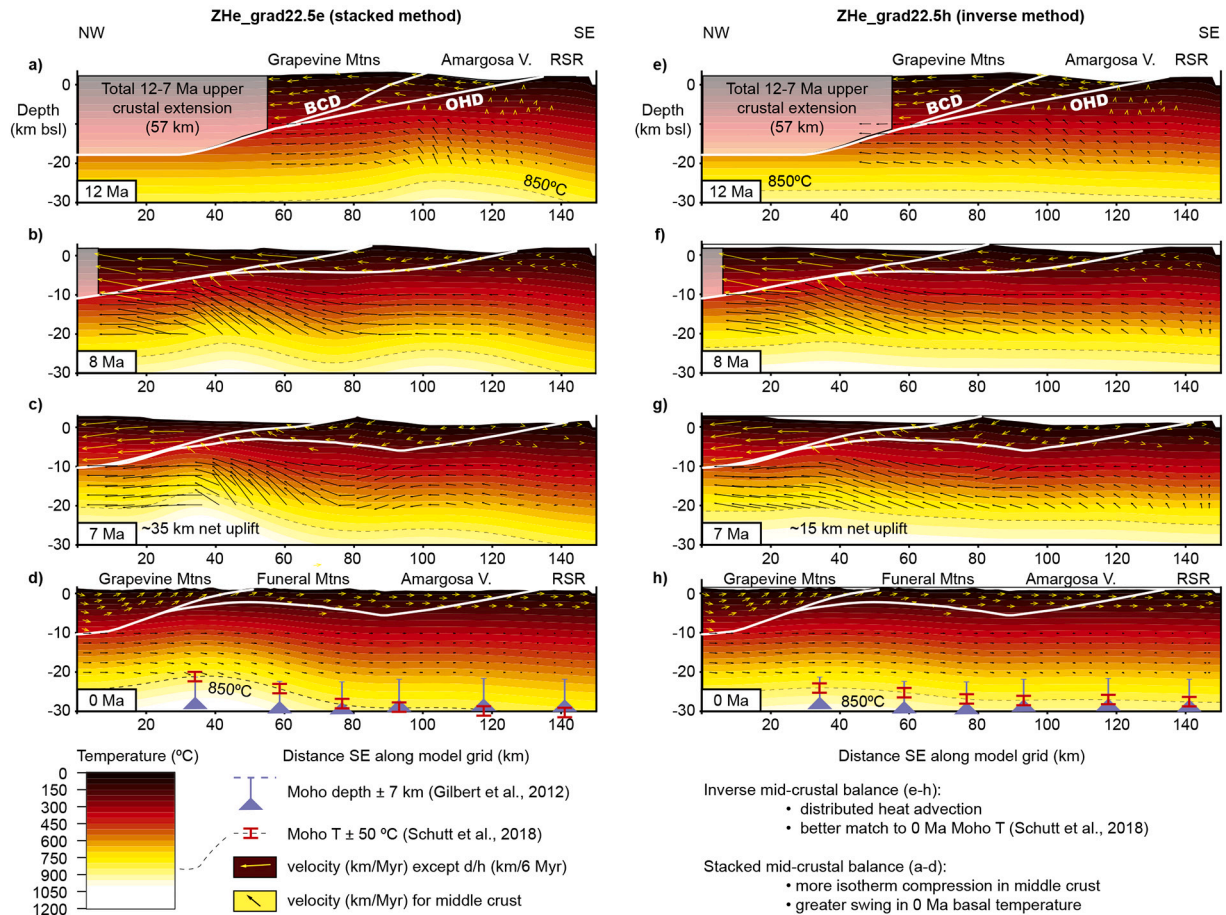


Fig. 7. Snapshots of thermo-kinematic model solutions for models ZHe_grad22.5e (a-d) and ZHe_grad22.5h (e-h), showing the evolution of temperature with advection using the stacked (a-d) vs inverse (e-h) mid-crustal area balancing scheme. The BCD and OHD are shown by solid white lines. Yellow and black arrows are incremental velocities for the upper and lower crust, respectively. Note maximum heat advection at 7 Ma (c and g), after which conductive cooling lowers the geotherm (d and h). Depth to the 850 °C isotherm is shown. See text for discussion of Moho depths and temperatures. (For interpretation of the references to colour in this figure legend, the reader is referred to the web version of this article.)

Table 3

Thermo-kinematic model parameter tests with best-fit model runs emboldened; see Fig. D.1 for plots of sensitivity tests.

Test Name	Balance scheme	UD	CD	Basal Boundary Condition	Thermal properties				40 Ma		16 Ma		0 Ma predicted model conditions		RSS of model ages	
					k	ρ	c	H	total Q	dT/dz	dT/dz	surface Q	Basal_T	40-0 Ma	12-0 Ma	
grad20f	Inverse	20	10	20 °C/km	2.4	2700	1100	0.4	60-61	22-24	29-37	62-89	820-910	529.9	67.1	
grad20g	Stacked	20	10	20 °C/km	2.4	2700	1100	0.4	60-61	22-24	25-41	60-98	720-980	514.4	66.8	
grad20h	Uniform	20	10	20 °C/km	2.4	2700	1100	0.4	60-61	21-24	28-38	67-91	790-930	518.3	65.9	
grad20i	Inverse	30	15	20 °C/km	2.4	2700	1100	0.4	60-61	22-24	25-45	60-108	725-1090	464.6	59.5	
grad20j	Stacked	30	10	20 °C/km	2.4	2700	1100	0.4	60-61	22-24	25-47	60-113	725-1130	414.0	53.3	
grad20k	Stacked	20	10	20 °C/km	2.4	2700	1100	0.4	60-61	22-24	25-42	60-101	725-1000	484.3	62.4	
gad20m	Stacked	20	10	20 °C/km	2.5	2700	1100	1.0	80-83	25-28	32-51	80-128	830-1140	503.5	30.0	
grad22.5c	Uniform	30	15	22.5 °C/km	2.0	2700	1100	1.0	75-78	29-33	37-65	74-130	960-1470	1377.2	76.3	
grad22.5d	Uniform	30	15	22.5 °C/km	2.5	2700	1100	0.4	60-26	24-26	28-49	70-123	800-1200	6.4	3.3	
grad22.5e	Stacked	20	10	22.5 °C/km	2.5	2700	1100	0.4	69-72	24-26	27-45	68-113	800-1080	12.1	9.6	
grad22.5f	Stacked	20	10	22.5 °C/km	2.5	2700	1100	0.0	56.25	22-24	23-39	58-98	725-980	2867.7	383	
grad22.5g	Stacked	20	10	22.5 °C/km	3.0	2700	1100	0.4	80-83	24-26	27-42	81-126	780-1030	102.7	16.8	
grad22.5h	Inverse	20	10	22.5 °C/km	2.5	2700	1100	0.4	69-72	24-26	31-40	78-100	900-1000	11.9	3.9	
grad22.5i	Uniform	20	10	22.5 °C/km	2.5	2700	1100	0.4	69-72	24-26	30-42	75-105	870-1020	11.0	3.8	
grad25e	Stacked	20	10	25 °C/km	2.4	2700	1100	0.4	72-75	27-29	30-51	72-122	880-1220	206.4	11.6	
grad25f	Stacked	20	10	25 °C/km	2.5	2700	1100	0.4	75-78	27-29	30-49	75-122	880-1190	161.2	8.6	
800c	Stacked	30	10	800 °C	2.4	2700	1100	1.0	87-90	24-26	30-40	72-96	800	119.3	7.0	
800d	Stacked	30	10	800 °C	2.0	2700	1100	1.0	78-81	24-26	31-42	62-84	800	291.3	17.7	
800e	Stacked	20	10	800 °C	2.5	2700	1100	0.4	72-75	24-26	27-35	68-87.5	800	198.3	34.0	
800g	Stacked	20	10	800 °C	2.5	2700	1100	1.0	>90	24-26	30-39	75-98	800	86.5	5.4	

All temperatures in °C; UD: upwelling depth (km), CD: compensation depth (km), Q: heat flow (mW m^{-2}), dT/dz.: geotherm (°C/km), RSS: residual sum of squares similarity test, k: thermal conductivity ($\text{W m}^{-1} \text{K}^{-1}$), ρ : density (kg m^{-3}), c: specific heat capacity ($\text{J kg}^{-1} \text{K}^{-1}$), H: radiogenic heat production ($\mu\text{W m}^{-3}$).

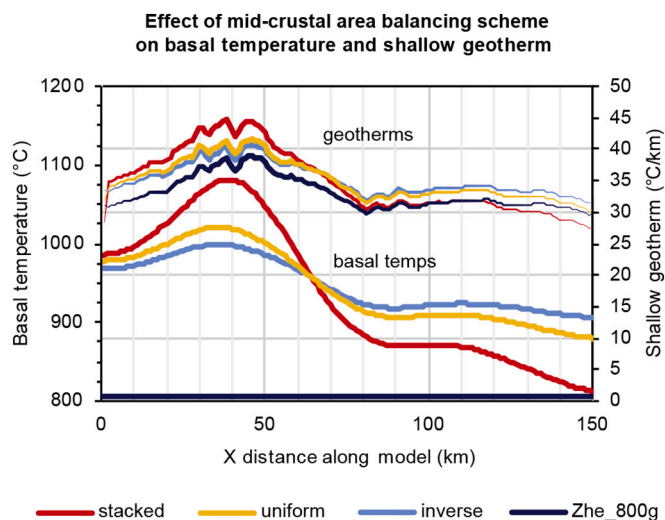


Fig. 8. Plots of 0 Ma modeled-predicted shallow geotherm (upper 2 km) and basal temperatures (30 km depth). Note the higher basal temperatures and geothermal gradients associated with the exhumed BCD footwall ($x = 20\text{--}60$ km). Rock and isotherm uplift are concentrated beneath exhumed detachment footwalls in the stacked scheme, yielding localized isotherm compression, whereas the inverse method distributes mid-crustal uplift more broadly, leading to less lateral basal temperature variation and less increase of the geothermal gradient beneath the Funeral Mountains.

cooling rates for the BCD footwall were recorded from ca. 11–7 Ma ($\sim 35\text{--}62$ °C/Myr), averaging ~ 42 °C/Myr for sites subjacent to the detachment, consistent with cooling rate of 41 °C/Myr estimated by Holm and Dokka (1991). From 7 to 0 Ma, BCD footwall samples were cooled at laterally-varying rates of 15 °C/Myr (in the northwest) to 1 °C/Myr (in the southeast). From 40 to 16 Ma, some samples were heated (~ 2.5 °C/Myr) then cooled (~ 1.5 °C/Myr), while others were monotonically cooled (~ 1.5 °C/Myr), depending on location (Fig. 11). Samples in the hanging walls of the ca. 40–16 Ma faults (compare Fig. 10a & b), corresponding to samples h–k of Beyene (2011) are among those that experienced model heating due to burial under 40–16 Ma strata (Figs. 3 & 10a/b), yet they remained hotter than 220 °C and thus were fully open to He-loss during that interval (Fig. 11). Most samples from the southeastern part of the BCD footwall (dark blue in Figs. 9–11) remained in the ZHe partial retention zone (140–200 °C; Wolfe and Stockli, 2010) for the duration of the model run, and thus were partially-reset from the prescribed 85 Ma inherited age. Modeled samples northwest of sample “m” (Beyene, 2011) (36.2 ± 1.6 Ma) (red to light blue in Figs. 9–11) begin the forward model run at temperatures > 220 °C, and thus they have zero age at model initiation, and the 85 Ma prescribed inherited age thus does not apply to them. Post-40 Ma model cooling ages are insensitive to the prescribed inherited age (see Fig. C.1).

4.2. Model cooling ages

For our preferred simulation ZHe_grad22.5 h, modeled cooling ages matched measured ages of Beyene (2011) very well (Fig. 9; RSS = 11.9), and other validity criteria were met (Table 3). Most ($\sim 95\%$; 19/20) parameter tests presented in replicate measured sample cooling ages < 12 Ma remarkably well (RSS < 80) (Table 3 & Appendix D), suggesting that *syn*-kinematic low-temperature cooling histories for detachment footwalls (e.g. fission track and (U-Th)/He) are much more sensitive to fault-controlled exhumation rates than to thermal boundary conditions or heat advection with footwall exhumation. This is illustrated in the RSS calculated using just a subset of samples cooled during or after BCD slip (post-12 Ma; $x = 47\text{--}61$ km in Fig. 9 & see Table 3). For parameter tests other than our preferred models, the full set of modeled samples

corresponding the Beyene (2011) sample sites have relatively poor fits (RSS > 150) to measured ZHe cooling ages ($x = 46\text{--}77$ km in Fig. 9). However, these tests yield good fits (RSS < 70) if pre-BCD cooling ages are excluded (such that $x = 47\text{--}61$ km in Fig. 9). This supports that, in areas with comparable pre-extensional geothermal gradients (25 ± 5 °C), ZHe ages from detachment footwalls should record faithfully the initiation of faulting (e.g. Stockli, 2005), though independent constraints on geological, kinematic, and thermal model inputs (and outputs) will increase the uniqueness of thermo-kinematic models (see Fox and Carter, 2020). Of the 20 model runs presented (Table 3), ZHe_grad22.5f is the only one that did not yield low RSS for the 12–0 Ma subset. This test differed from the very well-fit ZHe_grad22.5e (RSS = 12.1), only in its lack of heat production (Table 3). Thus, some heat production in the crust ($0.4\text{--}1.0$ mWm $^{-2}$) appears to be a requirement for matching the cooling ages and other model constraints.

Eocene-Oligocene muscovite $^{40}\text{Ar}/^{39}\text{Ar}$ cooling ages ($\sim 30\text{--}40$ Ma; Beyene, 2011) from the northwestern BCD footwall (Figs. 2b & 9) are compatible with tracked cooling histories in our thermo-kinematic models. When projected to the model cross-section and numerical grid, ca. 30 Ma and 35 Ma muscovite $^{40}\text{Ar}/^{39}\text{Ar}$ samples (Fig. 2b) (pseudo-plateau & total gas ages of Beyene, 2011) lie in the range $x = 49\text{--}50$ km (Fig. 9). Modeled samples from this location (and comparable, structurally-deeper ones farther northwest) cool through 350–425 °C, which is near the closure temperature for ^{40}Ar in muscovite considering low cooling rates modeled ($1\text{--}1.5$ °C/Myr; Fig. 11) and grain size (100–350 μm ; Beyene, 2011) (Harrison et al., 2009), between 29 and 40 Ma (Figs. 10a & 11). The cooling paths of northwestern-most modeled samples associated with the Eocene-Oligocene muscovite $^{40}\text{Ar}/^{39}\text{Ar}$ cooling ages (Beyene, 2011) thus support the validity of the thermo-kinematic model.

Model cooling histories for the BCD footwall also are compatible with the projected locations of pre-40 Ma muscovite $^{40}\text{Ar}/^{39}\text{Ar}$ cooling ages (Beyene, 2011). Southeast of sample “g” (Beyene, 2011 sample: 07FM38) in the BCD footwall, muscovite $^{40}\text{Ar}/^{39}\text{Ar}$ cooling ages are consistently older than 75 Ma (see Beyene, 2011). Our preferred thermo-kinematic models all predict that footwall locations southeast of sample location “g” (Beyene, 2011 sample 07FM38; Table 4) remained at temperatures < 350 °C for the duration of the run (light red to yellow and blue in Figs. 10 & 11), thus honoring these muscovite $^{40}\text{Ar}/^{39}\text{Ar}$ cooling ages.

5. Discussion

Our thermo-kinematic models produce validated stepwise reconstructions, constraining the evolution of both fault geometry and surrounding crustal thermal state (Figs. 7, 10, & 12). Along with other existing constraints (e.g. mid-crustal BCD-root zone, crustal thickness reconstructions), these inform models of 1) crustal structure associated with low-angle normal faulting (section 5.1), 2) the extent and longevity of a weak decoupling layer in the middle crust beneath the detachment fault system (section 5.2), 3) rheological feedbacks associated with thinning, cooling, and partial embrittlement of the weak layer (section 5.3), 4) mechanical development of the BCD (section 5.4), and 5) rarely observed high-magnitude seismicity on low-angle normal faults (section 5.5).

5.1. Crustal-scale structure of the BCD

The BCD initially (12 Ma) dipped 9–34° in the upper crust (average $\sim 29^\circ$), and was rooted into a gently ($< 15^\circ$) dipping plastic shear zone through the brittle-plastic transition (BPT) from $\sim 8\text{--}12$ km depth. Related shear at greater depth probably was delocalized, and was certainly delocalized below 15 km depth (Figs. 12 & 13). Overall, this is consistent with models in which upper and lower crustal deformation are decoupled along detachments (Spencer, 1984; Davis and Lister, 1988; Wernicke and Axen, 1988; Singleton and Mosher, 2012; Platt

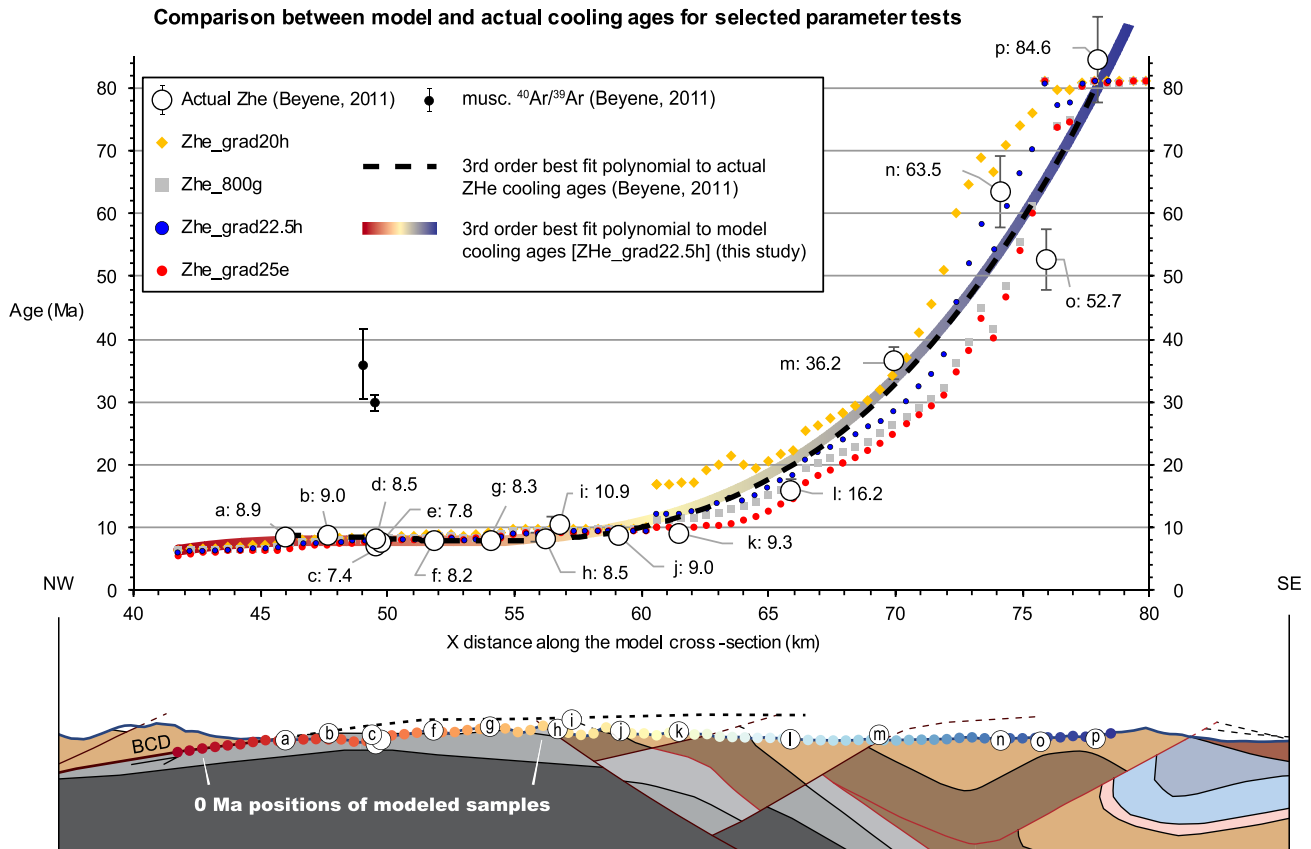


Fig. 9. FetKin-calculated (modeled) and actual (Beyene, 2011) BCD footwall ZHe cooling ages vs distance southeast along the model cross section. The cross section is an enlarged view centered on the Funeral Mountains MCC from Fig. 3a (0 Ma). The black dashed curve is a polynomial fit to actual ZHe ages (Beyene, 2011). The red-yellow-blue colour ramp curve is a polynomial fit to our preferred model test, ZHe_grad22.5 h. Modeled sample positions are shown on the cross-section with the symbol colour corresponding to the colour ramp polynomial (top), the sample positions Fig. 10, and the cooling history curves in Fig. 11. (For interpretation of the references to colour in this figure legend, the reader is referred to the web version of this article.)

et al., 2015; Deng et al., 2020), provided that a weak crustal layer exists (e.g. Clerc et al., 2015; Brun et al., 2018; Jolivet et al., 2018), but inconsistent with models in which detachments and their root shear zones transect the entire crust or lithosphere (Wernicke, 1985; Lister et al., 1986, 1991).

Kinematic reconstruction of ductile fabrics and microstructures subjacent to the BCD support the dip ranges presented above. Mica fish, stretching lineations, and mesoscopic folds in both quartz- and calc-mylonites that are linked kinematically to the BCD presently show mostly top-NW shear along a mean vector plunging 12° toward 120° (Hoisch and Simpson, 1993) (see 1b in Fig. 12). Some shallowly NW-plunging (toward $\sim 290^\circ$) stretching lineations in calc-mylonite also are reported by Hoisch and Simpson, 1993 and Beyene, 2011). Reconstruction of $\sim 25^\circ$ of late Miocene SE-tilting of the Funeral Mountains MCC (see Figs. 3, 10, & 12) rotates the mean shear direction ($12^\circ/120^\circ$; Hoisch and Simpson, 1993) to $\sim 13^\circ/300^\circ$ (in the plane of our section) (1a in Fig. 12), suggesting that the shear zone initially dipped 13° NW. This is consistent with our kinematic reconstruction, which shows a 14° dip in the BCD root zone.

Structurally deeper, high-temperature mylonites ($400\text{--}500^\circ\text{C}$), which may have been linked to the BCD, support that the BCD-related shear was delocalized and distributed below 12–15 km depth (see locations 2a & 2b in Fig. 12), depending on time-step. Some quartz grains in quartzite mylonites and mylonitic shear bands in schist were deformed by dynamic recrystallization mechanisms as high temperature as grain boundary migration (GBM) (Lima et al., 2018). This deformation mechanism, and prism $\langle a \rangle$ slip revealed in EBSD patterns of the top-NW mylonites (Sauer et al., 2013), support shearing during high temperature, low-stress conditions, in which the yield strength of

quartz-rich rocks is very low ($<10\text{--}20$ MPa) over a range of strain rates ($10^{-12}\text{--}10^{-15}$ s $^{-1}$) (Hirth et al., 2001; Stipp et al., 2002; Behr and Platt, 2011; Cooper et al., 2017; Tokle et al., 2019; Hughes et al., 2019). Platt and Behr (2011) inferred that a weak middle crust would produce distributed shear beneath the mylonite zone formed in the cooler, shallower BPT. Their model for shear zone thickness with depth predicts 2–6 km-thick zones of distributed shear (Fig. 12) in the quartz-rich middle crust, though the upper end of this range may be higher with thicker and hotter middle crust (Fig. 12). Deeper, in the mantle lithosphere, the distributed shear zones may be as wide as 50 km, depending on rheology and the presence of a gabbroic lower crust (Freed et al., 2007; Gueydan et al., 2014).

Below the localized-distributed transition (LDT: Cooper et al., 2010, 2017), strain in quartz-rich rocks is distributed by high-T, low-stress dynamic quartz recrystallization. We use the 500°C model isotherm (Fig. 12) to mark the LDT, which apparently was advected upward >6 km during footwall exhumation (in ZHe_grad22.5 h; greater in ZHe_22.5e) (it remains slightly deeper along the model boundaries). If detachments sole into the LDT (e.g., Cooper et al., 2017), then upper crustal extension most likely was decoupled from that in the lower crust and mantle lithosphere, and the depth of decoupling would have decreased with time as the LDT was advected (similar to downward-migrating BPT through nappe folds in Brun et al., 2018).

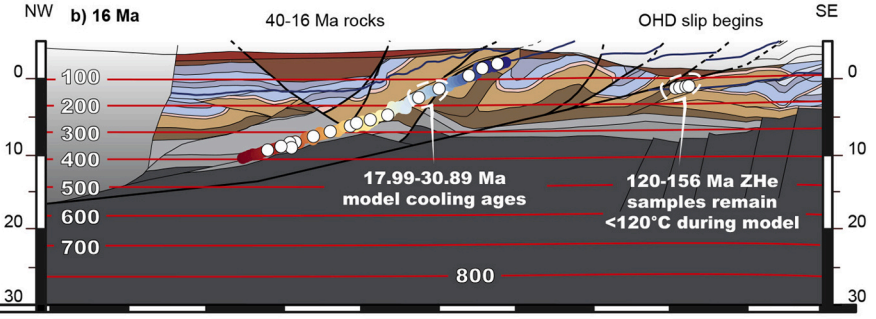
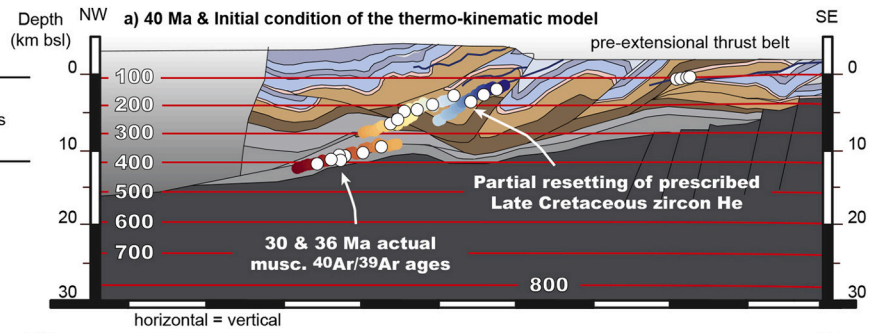
5.2. Mid-crustal flow

Our preferred thermo-kinematic models predict very high temperatures in the mid-lower crust prior to and during detachment faulting, consistent with a weak and partially-molten middle crust (Fig. 13). We

Forward thermo-kinematic models of detachment faulting in model cross-section

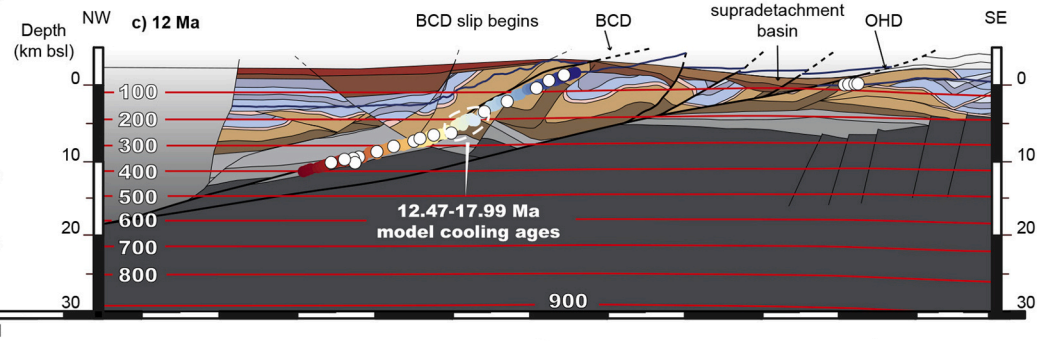
Actual Zircon (U-Th)/He ages (Beyene, 2011 & G. 2018)		Associated model Zircon (U-Th)/He ages (this study)	
q-t	120-156 Ma	61-82. Ma	
n-p	53-85 Ma	30.89 Ma	
m	36.2 ± 1.6 Ma	17.99 Ma	
l	16.2 ± 1.6 Ma	12.47 Ma	
k	9.3 ± 0.7 Ma	9.69 Ma	
j	9.0 ± 0.7 Ma	9.54 Ma	
i	10.9 ± 0.9 Ma	8.54 Ma	
h	8.5 ± 0.7 Ma	8.87 Ma	
f-g	8.2-8.3 ± 0.7 Ma	8.54 Ma	
e	7.8 ± 0.6 Ma	8.65 Ma	
d	8.5 ± 0.7 Ma	8.56 Ma	
c	7.4 ± 0.5 Ma	8.34 Ma	
b	9.0 ± 0.7 Ma	8.11 Ma	
a	8.9 ± 0.7 Ma	6.55 Ma	

— 300 — model isotherm in °C
 — normal fault



Key notes on 16-12 Ma:

- 3.9 mm/yr total horizontal extension on OHD and synthetic faults
- NsO deposited on PgNsT in SE Funeral Mtns; 12-11 Ma unconformity
- 15.4 km of 16-12 Ma extension on OHD and synthetic faults
- Bahadori et al. (2018) suggest >2500 m elevation in northwest



Key notes on 12-7 Ma:

- BCD rate = 7.5 mm/yr
OHD rate = 3.9 mm/yr
- NsN synorogenic rocks deposited on FMCC
- Basin inverted and eroded from ~7-0 Ma
- ~57 km of cumulative extension (11.4 mm/yr)

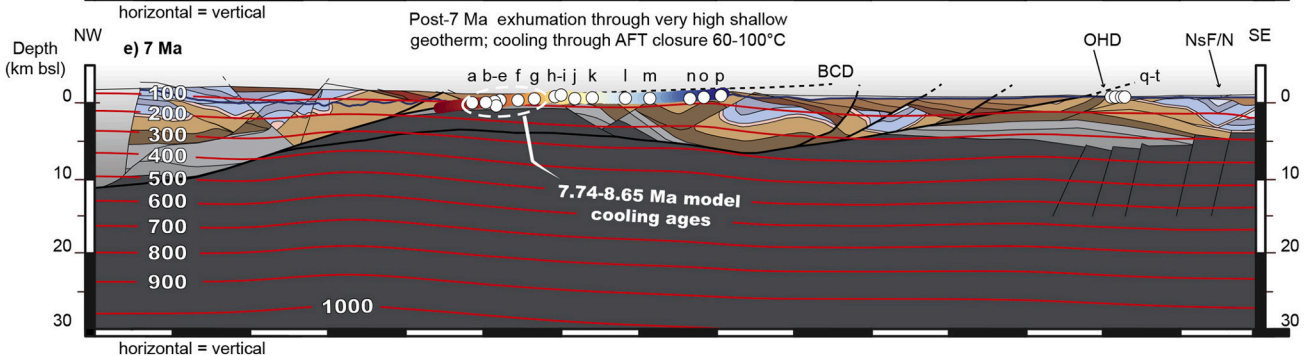
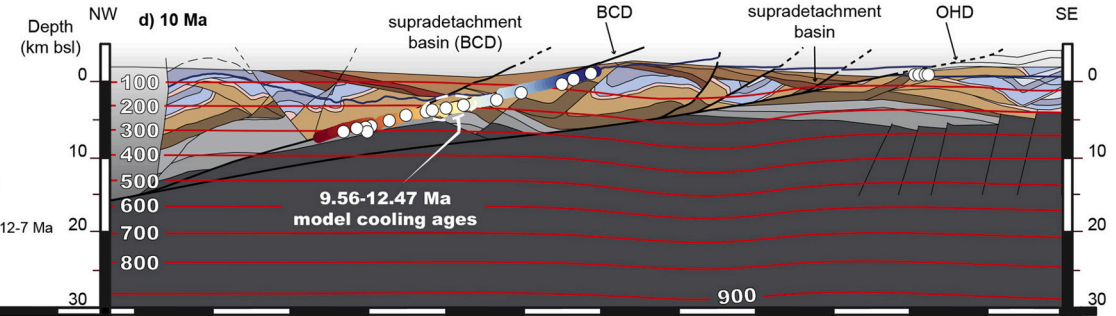


Fig. 10. Snapshots of our preferred forward thermo-kinematic model (ZHe_grad22.5 h; inverse balancing method) showing isotherm evolution and sample positions with detachment slip and footwall exhumation. a) Initial condition at 40 Ma. b) 16 Ma. c) 12 Ma. d) 10 Ma. e) 7 Ma. Key notes on each reconstruction sequence are detailed in the margin and the text. Abbreviations are the same as Fig. 2.

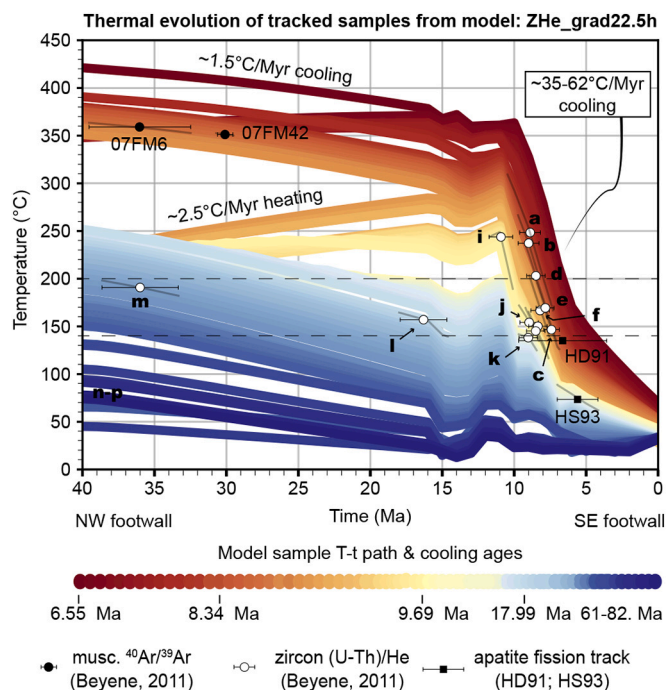


Fig. 11. Temperature-time evolution of modeled samples showing cooling and heating through time for different parts of the BCD footwall. Measured samples (white circles) (Beyene, 2011) are plotted along their respective cooling paths (colored curves) based on reconstructed locations (Figs. 3 & 9). Analytical age uncertainties for the measured samples (Beyene, 2011) are shown by grey lines parallel to the associated modeled cooling paths. Note that all measured sample ages plot on their respective model cooling paths, in temperature space, within uncertainty of the 140–200 °C ZHe partial retention zone (Wolfe and Stockli, 2010; Cai et al., 2020). Rapidly cooled samples (NW) generally record higher closure temperatures than slowly cooled samples.

Table 4
Zircon (U-Th)/He ages and model cooling ages for best-fit tests

Sample ID	Age	Sample name (this study)	associated model cooling ages (by model suffix)		
			800g	grad22.5h	grad22.5e
09FM15	8.9 ± 0.7	a	7.67	7.74	7.67
09FM8	9.0 ± 0.7	b	8.07	8.11	8.09
09FM9	7.4 ± 0.5	c	8.33	8.34	8.35
07FM43	8.5 ± 0.7	d	8.33	8.56	8.35
09FM10	7.8 ± 0.6	e	8.33	8.65	8.35
07FM8	8.2 ± 0.7	f	8.57	8.54	8.64
07FM38	8.3 ± 0.7	g	8.86	8.87	8.81
07FM13	8.5 ± 0.7	h	9.57	9.54	9.66
07FM15	10.9 ± 0.9	i	9.58	9.56	9.67
07FM10	9.0 ± 0.7	j	9.80	9.69	9.83
07FM34	9.3 ± 0.7	k	11.50	12.47	12.63
07FM29	16.2 ± 1.6	l	16.50	17.99	17.93
07FM27	36.2 ± 1.6	m	27.80	18.78	30.72
07FM26	63.5 ± 5.6	n	48.60	30.89	61.57
07FM24	52.7 ± 4.7	o	74.80	60.62	71.92
07FM21	84.6 ± 6.8	p	74.80	78.26	81.2
RS-2	128.5 ± 7.9	q	nc	nc	nc
RS-1	140.8 ± 13.2	r	nc	nc	nc
RS-3	147.1 ± 8.2	s	nc	nc	nc
RS-4	156.3 ± 7.8	t	nc	nc	nc

nc: not calculated

09FM & 07FM are from Beyene (2011)

RS- are from Giallorenzo et al. (2018)

infer that, initially, this weak middle crust decoupled upper crustal deformation from that in both the lower crust and mantle lithosphere (e.g. Wernicke, 1992; Lavier and Manatschal, 2006; Gueydan et al., 2008; Huismans and Beaumont, 2011; Brune et al., 2017) during detachment faulting from ca. 16–7 Ma, but was subsequently cooled (mostly below 600 °C) to promote post-7 Ma coupling of the crust to the mantle lithosphere (Wernicke, 1992; Harry et al., 1993; Péron-Pinvidic et al., 2013). Specifically, model temperatures are >600 °C at depths of 12–20 km during extension (16–7 Ma). Under these conditions, partially-molten quartz-rich crust could flow at very low shear stress (10–20 MPa) under lateral pressure gradients caused by focused upper crustal thinning (Fig. 13) and/or by lateral topographic gradients (Block and Royden, 1990; Kruse et al., 1991; Wdowinski and Axen, 1992; Beaumont et al., 2001; Rey et al., 2001; Grujic, 2006; Rey et al., 2009a/b; Whitney et al., 2013; Platt et al., 2015).

We estimate the thickness and longevity of the decoupling, weak layer (Fig. 13) using our stepwise thermo-kinematic models, crustal thickness reconstructions (Bahadori et al., 2018), gravity/tomographic studies (Hussein et al., 2011; Lee et al., 2014), and a crude area-balanced crustal section. Mid-Miocene crustal thickness along our transect was probably 50–60 km (Bahadori et al., 2018). Both gravity and tomographic models (Hussein et al., 2011; Lee et al., 2014) suggest ~10–15 km of gabbroic lower crust is present regionally beneath the Death Valley area (Fig. 13b), plus an additional 1–5 km of underplated basalt locally (identified beneath Death Valley). Based on our kinematic reconstructions and thermal models, then, the middle Miocene (~16 Ma) weak layer occupied the depth range between ~22 ± 3 km depth (600 °C isotherm) and ~40 ± 5 km depth (top of mafic lower crust) (Fig. 13a).

Thus, the weak mid-crustal layer was 10–26 km thick (Fig. 13). In the deeper parts of the weak layer (possibly at 30–45 km depth from 16 to 10 Ma), where temperatures were likely >800 °C, micaceous quartz-rich crust would be partially molten and highly fluid (Grujic, 2006), with effective viscosity ~10¹⁹ Pa s, while gabbroic lower crust may retain strength, with effective viscosity 10²⁰–10²¹ Pa s, assuming a strain rate of 10⁻¹⁴ s⁻¹ (Bürgmann and Dresen, 2008; Schutt et al., 2018). A fairly high pre- to *syn*-extensional crustal geothermal gradient (22–35°/km)

Reconstruction of plastic shear zones, principal stress orientations, and seismogenic thickness along the BCD

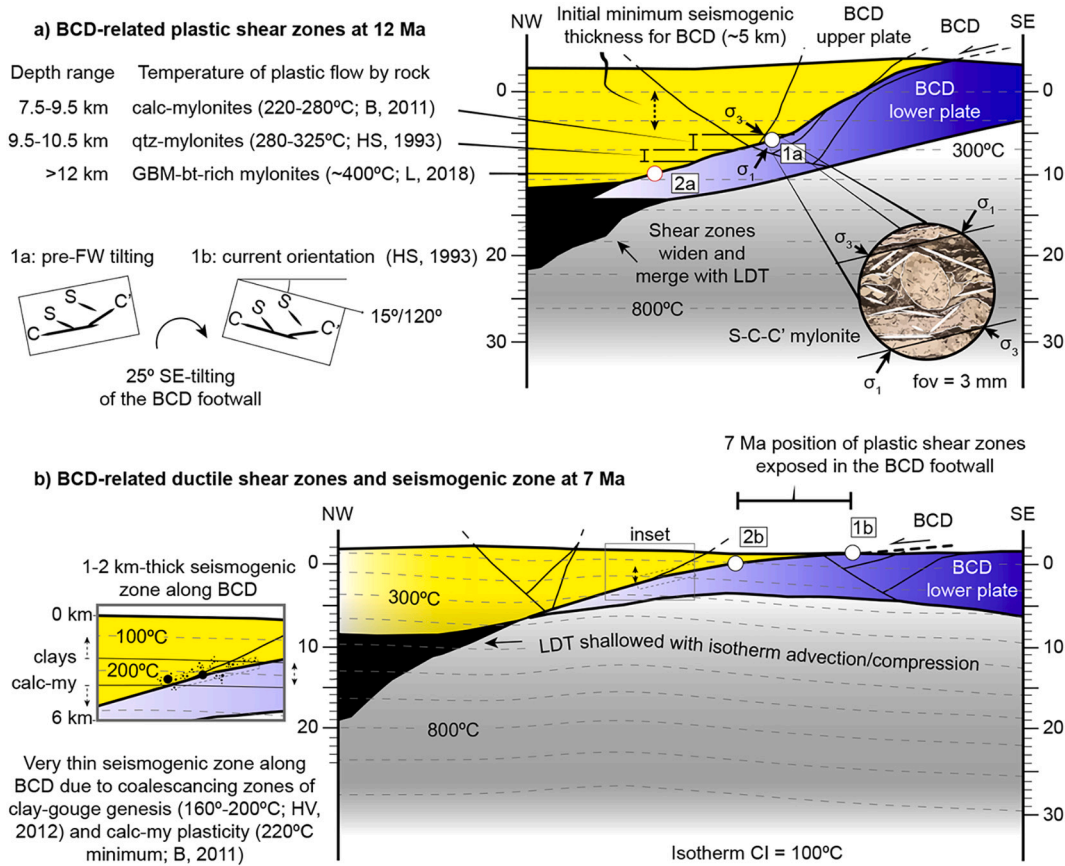


Fig. 12. Crustal-scale sections of the model at BCD initiation (a) and at end of BCD slip at 7 Ma (b). Both fabrics and temperatures of crystal-plastic deformation in calc-(1a/b), quartz-(1a/b), and biotite-rich (2a/b) mylonites along the BCD are after [Beyene \(2011\)](#) (B, 2011), [Hoisch and Simpson, 1993](#) (HS, 1993), and [Lima et al., 2018](#) (L, 2018), respectively. These plastic shear zones, currently exposed in the BCD footwall, are shown in their reconstructed positions along the BCD (white circles). The reconstructed seismogenic zones at 12 Ma and 7 Ma, shown by double-headed vertical arrows, are based solely upon temperature. See text for more discussion.

and a partially-molten, micaceous, quartz-rich middle crust are both consistent with major silicic volcanism in the region that immediately pre-dated and coincided with large- magnitude extension. Examples include the 16–11 Ma southwest Nevada Volcanic Field ([Sawyer et al., 1994](#)), 14–12 Ma Owshead Volcanic Field: ([Andrew and Walker, 2009](#); [Luckow et al., 2005](#)), and the ~11–9 Ma Shoshone Volcanics/Black Mountains Intrusive Suite ([Holm, 1995](#); [Calzia et al., 2016](#)).

The modeled thickness inferred for the weak mid-crustal layer supports a shallow isostatic compensation depth for heterogeneous upper crustal thinning (10–15 km), which is most consistent with the inversely weighted mid-crustal balancing scheme (Figs. 6, 7 & Table 3). With a 10–26 km-thick weak layer, previous workers suggested flow could be channelized over length-scales of 100–250 km (e.g. [Block and Royden, 1990](#); [Kruse et al., 1991](#); [McKenzie et al., 2000](#)), smoothing out lateral variations in upper crustal thinning over 1–2 Myr. We interpret this compensation as laterally-variable necking in the low-viscosity mid-crustal layer (general shear; Fig. 13b).

5.3. Thinning and cooling the weak layer: Implications for 4D rift evolution

As the middle crust was thinned, cooled, and partly embrittled beneath detachments, rocks migrated upward through mid-crustal rheological transitions (e.g., [Cooper et al., 2010](#); [Platt et al., 2015](#); [Cooper et al., 2017](#); [Brun et al., 2018](#)) until the weak layer was effectively removed. This process is similar to “occlusion” ([Wernicke, 1992](#))

or “annealing” ([Pérez-Gussinyé and Reston, 2001](#)) of the weak crust by both cooling and mechanical thinning (e.g. [Wernicke, 1992](#); [Harry et al., 1993](#)) (Fig. 13). [Wernicke \(1992\)](#) defined occlusion as juxtaposition of gabbroic lower crust beneath brittle (but previously ductile) upper crust, caused by flow and exhumation of the weak layer toward uplifting MCCs. [Pérez-Gussinyé and Reston \(2001\)](#) described hyperextension, cooling, and complete embrittlement of the ductile lower crust following reduction of crustal thickness to <10 km, in reference to magma-poor rifted margins. We envision similar processes, but our modeling incorporates both thinning and cooling of the deep weak layer as well as exhumation and embrittlement of the stronger, shallower ductile middle crust (Fig. 13). However, our models do not require juxtaposition of gabbroic lower crust immediately beneath brittle crust ([Wernicke, 1992](#)) or complete embrittlement of the lower crust (e.g. [Pérez-Gussinyé and Reston, 2001](#); [Péron-Pinvidic et al., 2013](#)).

Thinning, cooling, and exhumation of the weak layer apparently creates an intraplate rheological feedback that enhances coupling between the strong upper crust and mantle lithosphere (e.g. [Wernicke, 1992](#); [Harry et al., 1993](#)) (see conceptual strength profiles in Fig. 13). Enhanced crust-mantle coupling promotes, in turn, narrower strain localization (e.g. [Buck, 1991](#); [Gueydan et al., 2008](#); [Gueydan and Précigout, 2014](#)) and has been suggested to cause stronger viscous coupling between the lithosphere and asthenosphere ([Reston, 1990a/b](#); [Jolivet et al., 2018](#)). In contrast to the decoupled, detachment-dominated phase of extension, the modern lithosphere in southeastern California is now thinned and mechanically coherent, similar to the

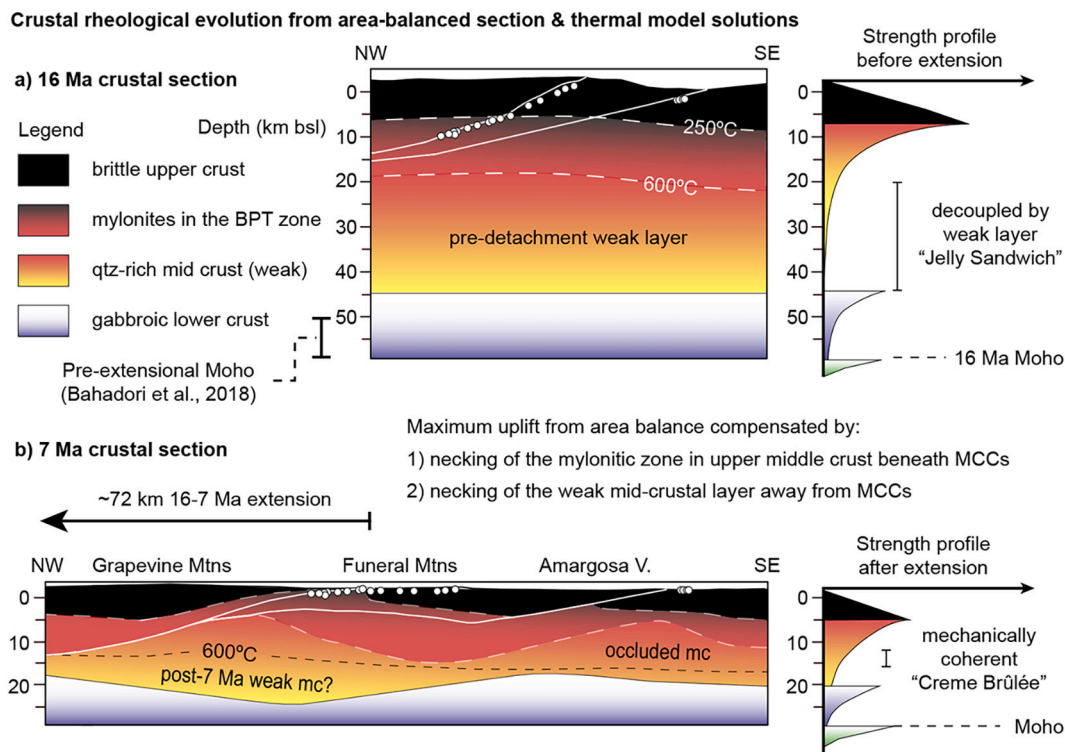


Fig. 13. Crustal-scale area-balanced sections showing conceptualized thermo-rheological evolution and strain partitioning during large-magnitude extension from 16 Ma (top) to 7 Ma (bottom). Concept adapted from Wernicke (1992); his Figs. 8 & 9) to match our modeled temperatures and kinematics. Initial rheological layers are defined by model isotherms, crustal thickness reconstruction (Bahadori et al., 2018), and gabbroic lower crust thickness from modern P-wave tomography (Lee et al., 2014) and gravity modeling (Hussein et al., 2011). Conceptual strength profiles are loosely based on Wernicke (1992) and Jackson (2002), assuming a 10^{-14} s^{-1} strain rate and our model geotherms. Solid white lines indicate the BCD and OHD. White circles are reconstructed thermochronometry samples (Beyene, 2011). Approximately 20% of the weak mid-crustal area at 16 Ma is missing at 7 Ma, which we attribute 3D flow of the weak middle crust out of the section plane, melting and eruption of mid-crustal silicic magmas, and/or inaccurate paleo-crustal thickness estimates. lc: lower crust, mc: middle crust, uc: upper crust. BPT: brittle-plastic transition.

“crème brûlée” model of lithospheric strength (Jackson, 2002; Burov and Watts, 2006) (Fig. 13). In particular, recent studies of mantle xenoliths (Behr and Hirth, 2014; Bernard and Behr, 2017; Chatzaras et al., 2015), mantle seismic anisotropy (Barbot, 2020), and post-seismic relaxation (Shaozhuo Liu et al., 2021) in southeastern California (within and near our study area as defined by Fig. 1) all support the existence of a vertically mechanically coherent lithosphere that is at least moderately coupled to asthenospheric flow. That is, stresses applied by gravitational potential forces, plate boundary shear, and basal mantle shear tractions appear to be transmitted between the mantle lithosphere and the crust in a fairly narrow zone of transtension (50–100 km) within the Eastern California Shear Zone (Behr and Hirth, 2014; Chatzaras et al., 2015; Dixon and Xie, 2018; Liu et al., 2021). The modern, mechanically-coupled lithosphere there may have resulted directly from thinning, cooling, and partial embrittlement of the weak layer regionally (Wernicke, 1992; Harry et al., 1993; Pérez-Gussinyé and Reston, 2001) (Fig. 13).

Evolving coupling strength between different rheological layers in the lithosphere strongly influences the geodynamic evolution of continental rifts, MCC exhumation, and magma-poor rifted margins (e.g. Buck, 1991; Pérez-Gussinyé and Reston, 2001; Wijns et al., 2005; Lavier and Manatschal, 2006; Mohn et al., 2012; Péron-Pinvidic et al., 2013; Naliboff and Buitier, 2015; Labrousse et al., 2016; Jolivet et al., 2018; Korchinski et al., 2018; Osmundsen and Péron-Pinvidic, 2018; Chenin et al., 2020). Models of magma-poor rifted-margin evolution predict an ocean-ward migrating locus of strain on faults and shear zones, in which upper crustal extension is balanced by lower crustal flow during the stretching and thinning phases (Péron-Pinvidic et al., 2013; Brune et al., 2014). Necking of the full (remaining) crustal thickness proceeds after

the flowing mid-lower crustal material thins and cools to the point of embrittlement and mechanical coupling (Pérez-Gussinyé and Reston, 2001). Shear zones in the upper crust are then thought to interact with those in the lower crust and mantle lithosphere during coupled hyperextension (Reston, 2009; Mohn et al., 2012; Péron-Pinvidic et al., 2013; Brune et al., 2014; Naliboff et al., 2017).

The transition between thinning and hyperextension is facilitated by “annealing” the weak layer (Pérez-Gussinyé and Reston, 2001) with reference to magma-poor rifted margins, and is not much different from “occlusion” (Wernicke, 1992), applied to MCCs. Occlusion of the weak layer was likely reached at ca. 7–6 Ma in an ~200 km-long north-south belt of MCCs around our model transect (Fig. 1), when ductile middle crust was exhumed beneath detachment faults regionally (Holm and Dokka, 1991, 1993; Hoisch and Simpson, 1993; Oldow et al., 1994; Hoisch et al., 1997; Beyene, 2011; Bidgoli et al., 2015a; Sizemore et al., 2019). This timing coincides well with an east-to-west migration in the locus of regional upper-crustal extension (e.g. Snow et al., 1999; Monastero et al., 2002; Walker et al., 2014) away from the MCC belt, similar to ocean-ward younging normal fault systems along magma-poor margins (Reston and McDermott, 2011).

Changes in deformation style and locus following footwall exhumation in MCCs suggests that occlusion is common and that it changes the integrated mechanical behavior of the lithosphere. Late Miocene exhumation of MCCs in the western salient of the USA MCC belt (Fig. 1) suggests close temporal association of weak layer annealing and onset of strong coupling both within the lithosphere and between the lithosphere and asthenosphere (Behr and Hirth, 2014; Chatzaras et al., 2015; Dixon and Xie, 2018; Barbot, 2020; Liu et al., 2021). Similarly, west- and southwest-migration of Miocene-Pliocene strain and younger high-angle

faults overprinting back-tilted detachments may have occurred in both the lower Colorado River extensional corridor (e.g. Singleton, 2015; Zuza et al., 2019; Thacker et al., 2020) and northern Basin and Range province (e.g. Wernicke, 1992; Harry et al., 1993), following mid-crustal exhumation beneath regional detachments there. Overprinting fault relationships in the Menderes MCC of western Anatolia (Oner and Dilek, 2013) suggest that occlusion-like processes may have operated there as well.

5.4. Stress-rotations in the brittle-plastic transition zone: Mechanical implications for low-angle normal fault initiation

The reconstructed orientations of the BCD-related mid-crustal shear zones (Fig. 12) allows inference of the maximum principal stress orientation near the base of the brittle crust, which informs models for detachment fault slip and initiation. Because plastic shear zones lie at $\sim 45^\circ$ to the maximum principal stress σ_1 , and given the dip range discussed above, we suggest that σ_1 plunged $65^\circ \pm 7^\circ$ NW in the calc-mylonitic root zone of the BCD (~ 220 – 325°C ; \sim Fig. 11) (including currently subhorizontal and gently NW-dipping shear zone fabrics in our section plane; Hoisch and Simpson, 1993; Beyene, 2011); it may have plunged less steeply where the biotite-rich mylonites and GBM-dominated quartz shear bands formed (Fig. 12). This assumes that our cross-section plane is perpendicular to σ_2 . Similar stress orientations were derived empirically for the Whipple detachment fault (σ_1 plunge of 61 – 71° NE; Axen, 2020), based on fault dip ranges, paleopiezometry (Behr and Platt, 2011) and fluid inclusion studies of the fault rocks (Selverstone et al., 2012). Stress rotation also is inferred commonly for other detachment faults based on their reconstructed low angles of initiation and high-strength fault rocks (see Axen, 2004; Collettini, 2011).

However, it is unclear what causes stress rotations and whether they are a local or regional phenomenon. Localized stress rotations produced by mechanical anisotropy are documented in plastic shear zones (e.g. Treagus, 1973; Wells, 2001), inferred for fractured damage zones surrounding brittle faults (e.g. Faulkner et al., 2006), and between sedimentary lithologies (Casey, 1980; Bradshaw and Zoback, 1988). These could be exaggerated by permeability anisotropy associated with foliations, fractures, and microcracks, depending on their orientation (Healy, 2009). Crustal scale stress rotations have been produced in layered and elastic numerical models. Melosh (1990) used layered models to show that regional-scale stress rotations are a natural consequence of a low-viscosity lower crust and high strain rate. Elastic numerical models have also generated stress rotations by applying asymmetrical boundary forces, appealing to calling on mid- to lower-crustal flow-induced basal shear traction (Yin, 1989; Harry et al., 1993; Westaway, 1999) or lateral gradients in vertical basal traction due to a crustal root (Spencer and Chase, 1989).

Tectonic-based quantification of asymmetric boundary forces that may rotate the stress field regionally have been limited. Axen (2020) showed that top-NE basal shear (due to Orocochia Schist exhumation) or dynamic buoyancy (due to appearance of a slab-free window) could have rotated stresses regionally in MCCs of the lower Colorado River extensional corridor (Fig. 1). Combined plate kinematic and volcanic field reconstructions place a slab window beneath the Death Valley area at ~ 12 – 10 Ma (Atwater and Stock, 1998; Dickinson, 2002), about when major detachment faults initiated there (Wernicke et al., 1988; Holm and Dokka, 1991, 1993; Hoisch and Simpson, 1993; Oldow et al., 1994; Hoisch et al., 1997; Beyene, 2011; Bidgoli et al., 2015a; Sizemore et al., 2019). Furthermore, continent-scale topographic reconstructions (Zhou and Liu, 2019) suggest that, from 20 to 0 Ma, dynamic topography in the Death Valley-Las Vegas area (Fig. 1) increased from 0 to 1000 m during a monotonic overall decrease in elevation. This suggests that the asthenospheric flow-driven vertical buoyancy force model of Axen (2020) may apply to the Death Valley region, and that stress rotations were regional. Stress-rotation in the deep brittle crust (of the modern

western USA) is supported by low-angle (30° – 35°) moment tensor solutions associated with the 2020 $M_w = 5.7$ Magna, Utah earthquake, which ruptured the province-bounding, listric Wasatch fault (Pang et al., 2020).

5.5. Shallow brittle-plastic transition and thin seismogenic zone along exhumed detachments

Rapid footwall uplift beneath detachment faults may advect sufficient heat to thin significantly the seismogenic zone as defined by temperature, possibly contributing to the lack of observed seismicity along active but partly exhumed detachments globally (Jackson and White, 1989; Wernicke, 1995; Collettini, 2011; Styron and Hetland, 2014). Our preferred thermo-kinematic models (Table 3) all suggest that the active upper BPT, corresponding to the depths between the 250°C and 325°C isotherms, was uplifted 4–5 km during rapid BCD footwall exhumation from 12 to 7 Ma (Fig. 12). The BPT along the BCD was elevated from ~ 7.5 – 9.5 km to 4–5 km over 5-Myr (Fig. 12b). Subsequent conductive cooling from 7 to 0 Ma increased the depth of the BPT to ~ 6 – 7 km (compare Fig. 7g & h). The shallow BPT predicted by our forward models is supported by the geophysics-based analytical models of Zuza and Cao (2020), which found an inverse correlation between surface heat flow and seismogenic thickness.

Thinning of the seismogenic zone along the BCD by uplift of its base likely was augmented by development of creep-prone, weak minerals along the shallow portion of the fault, which probably lowered the top of the seismogenic zone (Collettini and Sibson, 2001; Collettini, 2011). These processes may explain the apparent absence of large-magnitude earthquakes on exhumed detachment faults globally. Along the BCD, the zones of shallow, weak fault creep and crystal-plastic strain (especially in carbonates) may have nearly coalesced (Fig. 12b). The BCD locally displays 1–10 m of foliated, clay-rich gouge at the base of the upper plate (Hoisch, pers. comm.; Lutz et al., 2019), suggesting that creep probably characterized the shallow BCD sections. Weak clays are stable up to 160 – 200°C (Haines and van der Pluijm, 2012) and may exhibit velocity strengthening behavior up to 250°C (Hartog Den et al., 2012; Hartog Den et al., 2013; Hartog Den and Spiers, 2013); strain softening in calc-mylonites, which are common in the uppermost BCD footwall, flowed at temperatures as low as 220°C (Beyene, 2011) (Fig. 12). This suggests that, at times, no part of the BCD could nucleate large earthquakes. However, seismic ruptures can propagate both down into the BDT zone (Scholz, 2002; Aharonov and Scholz, 2018, 2019) and up through velocity-strengthening fault patches (e.g. Collettini et al., 2019). The early BCD, before significant uplift and heat advection, may have failed seismogenically at a low-angle in the deep brittle crust, similar to active examples low-angle normal faults in southern Tibet (Monigle et al., 2012), the northern Basin and Range (Pang et al., 2020), southeastern Papua New Guinea (Biemiller et al., 2020a/b; Cummins et al., 2020; Mizera et al., 2020), and other extensional systems globally (Abers, 2001).

In contrast, the seismogenic zone thickness relevant to faults in detachment upper plates may be greater than that along detachments themselves. Formation of foliated clay gouges is more prevalent along large-displacement faults (e.g. Rowe and Griffith, 2015) than along smaller-offset faults, due to increased fault-related damage and fluid flow with slip. Thus, top-down thinning of the seismogenic zone by formation of clay gouge may not occur on modest-displacement upper-plate normal faults that are common above detachments. We believe this may have been the case along the BCD. This disparity in fault rock architecture may contribute to the predominance of steep normal fault earthquakes in compilations (e.g. Jackson and White, 1989). Some foliated clay gouges are derived, at least in part, from detrital and authigenic clays present in sedimentary protoliths (e.g. van der Pluijm et al., 2001; Haines and van der Pluijm, 2008; Haines et al., 2009; Haines and van der Pluijm, 2012). This likely was true along the base of the BCD upper plate, which is a thick, clastic, passive margin sedimentary

sequence (see stratigraphic sections in Fig. 3 & Fig. B.2). Upper-plate faults have not been described in adequate detail to address this issue in our study area.

6. Conclusions

We present the first regional-scale, cross-sectional thermo-kinematic models of extensional detachment faulting globally (that we know of). Stepwise, iteratively achieved reconstructions of fault geometry and crustal thermal state yield model footwall cooling histories consistent with ZHe thermochronometric data (Beyene, 2011) (Figs. 9–11; Table 4). The stepwise reconstructed geometry and thermal state of our cross section (Fig. 10) reveal the kinematic and rheological evolution of the detachments and surrounding crust (Figs. 12 & 13), respectively, during continental rifting. These are used to inform conceptual models for large-magnitude crustal extension and detachment fault mechanics. The following conclusions are reached:

- 1) Two detachment faults in the Death Valley region, California, USA (the BCD and OHD) initiated and slipped at low angles (9–34°), accommodating ~72 km of NW-directed extension from 16 to 7 Ma; ~57 km of which accrued from ~12–7 Ma (11.4 mm/yr horizontal extension rate).
- 2) The detachment faults almost certainly soled initially into the top of a 15–26 km-thick layer of weak, quartz-rich middle crust that decoupled heterogeneous upper crustal extension from both the lower crust and mantle lithosphere, inconsistent with models of normal-sense simple shear of the whole lithosphere.
- 3) The weak, quartz-rich middle crust largely cooled through the 600 °C isotherm by ~7 Ma, effectively ending decoupling behavior and likely increasing mechanical coupling of the lithosphere.
- 4) Thinning and cooling of the weak layer at ~7 Ma coincided with a westward migration in the locus of transtension regionally, supporting that this process mediates intraplate strain patterns (e.g., Wernicke, 1992).
- 5) The BCD footwall cooled at a maximum rate of 35–62 °C/Myr during rapid (~7.5 mm/yr) slip, and upward heat advection raised the geotherm locally to 40 °C/km subjacent to the detachment, shallowing the top of brittle-plastic transition to ~4–5 km depth.
- 6) A thin seismogenic zone associated with the shallow brittle-plastic transition and development of weak, creep-prone, clay-rich fault rocks along detachments helps explain the lack of large historical earthquakes on active low-angle normal faults.
- 7) The reconstructed attitudes of plastic shear zones along the BCD indicate rotation of the maximum principal stress away from vertical, which, we speculate was caused by mantle flow through a slab window that appeared beneath the study area at ~12 Ma, when detachment faults initiated regionally.

Declaration of Competing Interest

The authors declare that they have no known competing financial interests or personal relationships that could have appeared to influence the work reported in this paper.

Acknowledgements

This work was supported by National Science Foundation grants EAR-1516680 (Lutz, Axen, and van Wijk) and EAR-061009 (Beyene, Wells, and Stockli), a Travel Grant from the New Mexico Institute of Mining and Technology Graduate Student Association (Lutz), and by the New Mexico Bureau of Geology and Mineral Resources (Ross). Move software was donated by PetroleumExperts, Houston. We thank Ecopetrol for use of and developmental support for FETKin. We are grateful to Thomas Hoisch and Alexander Robinson for their constructive reviews.

Appendix A. Supplementary data

Supplementary data to this article can be found online at <https://doi.org/10.1016/j.tecto.2021.228755>.

References

- Abers, G.A., 2001. Evidence for seismogenic normal faults at shallow dips in continental rifts. *Geol. Soc. 187* (1), 305–318. London, Special Publications.
- Aharonov, E., Scholz, C.H., 2018. A physics-based rock friction constitutive law: Steady state friction. *J. Geophys. Res. Solid Earth* 123 (2), 1591–1614.
- Aharonov, E., Scholz, C.H., 2019. The brittle-ductile transition predicted by a physics-based friction law. *J. Geophys. Res. Solid Earth* 124 (3), 2721–2737.
- Almendral, A., Robles, W., Parra, M., Mora, A., Ketcham, R.A., Raghieb, M., 2015. FetKin: Coupling kinematic restorations and temperature to predict thrusting, exhumation histories, and thermochronometric ages: Coupling Kinematic Restorations and Temperature. *AAPG Bull.* 99 (8), 1557–1573.
- Andrew, J.E., Walker, J.D., 2009. Reconstructing late Cenozoic deformation in central Panamint Valley, California: Evolution of slip partitioning in the Walker Lane. *Geosphere* 5 (3), 172–198. <https://doi.org/10.1130/GES00178.1>.
- Applegate, J.D.R., Hodges, K.V., 1995. Mesozoic and Cenozoic extension recorded by metamorphic rocks in the Funeral Mountains, California. *Geol. Soc. Am. Bull.* 107, 1063–1076. [https://doi.org/10.1130/0016-7606\(1995\)107<1063:macerbr>2.3.co;2](https://doi.org/10.1130/0016-7606(1995)107<1063:macerbr>2.3.co;2).
- Applegate, J., Walker, J.D., Hodges, K.V., 1992. Late cretaceous extensional unroofing in the Funeral Mountains metamorphic core complex. *Calif. Geol.* 20 (6), 519–522.
- Atwater, T., Stock, J., 1998. Pacific-North America plate tectonics of the neogene Southwestern United States: An update. *Int. Geol. Rev.* 40 (5), 375–402. <https://doi.org/10.1080/00206819809465216>.
- Axen, G.J., 2004. Mechanics of low-angle normal faults. In: Karner, G.D., Taylor, B., Driscoll, N.W., Kohlstedt, D.L. (Eds.), *Rheology and Deformation of the Lithosphere at Continental Margins*. Columbia University Press, New York Chichester, West Sussex (47 p).
- Axen, G.J., 2020. How a strong low-angle normal fault formed: The Whipple detachment, southeastern California. *GSA Bull.* 132 (9–10), 1817–1828.
- Bahadori, A., Holt, W.E., Rasbury, E.T., 2018. Reconstruction modeling of crustal thickness and paleotopography of western North America since 36 Ma. *Geosphere* 14, 1207–1231. <https://doi.org/10.1130/GES01604.1>.
- Barbot, S., 2020. Mantle flow distribution beneath the California margin. *Nat. Commun.* 11, 1–14.
- Batt, G.E., Braun, J., 1999. The tectonic evolution of the Southern Alps, New Zealand: insights from fully thermally coupled dynamical modelling. *Geophys. J. Int.* 136, 403–420. <https://doi.org/10.1046/j.1365-246x.1999.00730.x>.
- Beaumont, C., Jamieson, R.A., Nguyen, M.H., Lee, B., 2001. Himalayan tectonics explained by extrusion of a low-viscosity crustal channel coupled to focused surface denudation. *Nature* 414, 738–742. <https://doi.org/10.1038/414738a>.
- Behr, W.M., Hirth, G., 2014. Rheological properties of the mantle lid beneath the Mojave region in southern California. *Earth Planet. Sci. Lett.* 393, 60–72. <https://doi.org/10.1016/j.epsl.2014.02.039>.
- Behr, W.M., Platt, J.P., 2011. A naturally constrained stress profile through the middle crust in an extensional terrane. *Earth Planet. Sci. Lett.* 303, 181–192. <https://doi.org/10.1016/j.epsl.2010.11.044>.
- Bernard, R.E., Behr, W.M., 2017. Fabric heterogeneity in the Mojave lower crust and lithospheric mantle in Southern California. *J. Geophys. Res.* 122, 5000–5025. <https://doi.org/10.1002/2017JB014280>.
- Beyene, M.A., 2011. Mesozoic Burial, Mesozoic and Cenozoic Exhumation of the Funeral Mountains Core Complex, Death Valley, Southeastern California. PhD Thesis; 363 p. University of Nevada, Las Vegas.
- Bigoli, T.S., Amir, E., Walker, J.D., Stockli, D.F., Andrew, J.E., Caskey, S.J., 2015a. Low-temperature thermochronology of the Black and Panamint mountains, Death Valley, California: Implications for geodynamic controls on Cenozoic intraplate strain. *Lithosphere* 7, 473–480. <https://doi.org/10.1130/L406.1>.
- Bigoli, T.S., Amir, E., Walker, J.D., Stockli, D.F., Andrew, J.E., Caskey, S.J., 2015b. Low-temperature thermochronology of the Black and Panamint mountains, Death Valley, California: Implications for geodynamic controls on Cenozoic intraplate strain. *Lithosphere* 7 (4), 473–480. <https://doi.org/10.1130/L406.1>.
- Biemiller, J., Boulton, C., Wallace, L., Ellis, S., Little, T., Mizera, M., Niemeijer, A., Lavier, L., 2020a. Mechanical implications of creep and partial coupling on the World's Fastest slipping low-angle normal fault in Southeastern Papua New Guinea. *J. Geophys. Res. Solid Earth* 125 (10) (p. e2020JB020117).
- Biemiller, J., Taylor, F., Lavier, L., Yu, T.L., Wallace, L., Shen, C.C., 2020b. Emerged coral reefs record holocene low-angle normal fault earthquakes. *Geophys. Res. Lett.* 47 (20) (doi: e2020GL089301).
- Blackwell, D., Richards, M., Frone, Z., Batir, J., Ruzo, A., Dingwall, R., Williams, M., 2011. Temperature-at-Depth Maps for the Conterminous US and Geothermal Resource Estimates. Southern Methodist University Geothermal Laboratory.
- Blakely, R.J., Jachens, R.C., Calzia, J.P., Langenheim, V.E., 1999. Cenozoic basins of the Death Valley extended terrane as reflected in regional-scale gravity anomalies. In: Wright, L.A., Troxel, B.W. (Eds.), *Cenozoic Basins of the Death Valley Extended Terrane as Reflected in Regional-Scale Gravity Anomalies*, pp. 1–16.
- Block, L., Royden, L.H., 1990. Core complex geometries and regional scale flow in the lower crust. *Tectonics* 9, 557–567. <https://doi.org/10.1029/tc009i004p00557>.
- Bradshaw, G.A., Zoback, M.D., 1988. Listric normal faulting, stress refraction, and the state of stress in the Gulf Coast basin. *Geology* 16 (3), 271–274.

- Brun, J.-P., Sokoutis, D., Tirel, C., Gueydan, F., Van Den Driessche, J., Beslier, M.-O., 2018. Crustal versus mantle core complexes. *Tectonophysics* 746, 22–45. <https://doi.org/10.1016/j.tecto.2017.09.017>.
- Brune, S., Heine, C., Pérez-Gussinyé, M., Sobolev, S.V., 2014. Rift migration explains continental margin asymmetry and crustal hyper-extension. *Nat. Commun.* 5, 855. <https://doi.org/10.1038/ncomms5014>.
- Brune, S., Heine, C., Clift, P.D., Pérez-Gussinyé, M., 2017. Rifted margin architecture and crustal rheology: reviewing Iberia-Newfoundland, Central South Atlantic, and South China Sea. *Mar. Pet. Geol.* 79, 257–281. <https://doi.org/10.1016/j.marpetgeo.2016.10.018>.
- Buck, W.R., 1988. Flexural rotation of normal faults. *Tectonics* 7, 959–973. <https://doi.org/10.1029/tc007i005p0959>.
- Buck, W.R., 1991. Modes of continental lithospheric extension. *J. Geophys. Res.* 96, 20161–20178. <https://doi.org/10.1029/91jb01485>.
- Bürgmann, R., Dresen, G., 2008. Rheology of the lower crust and upper mantle: evidence from rock mechanics, geodesy, and field observations. *Annu. Rev. Earth Planet. Sci.* 36, 531–567.
- Burov, E.B., Watts, A.B., 2006. The long-term strength of continental lithosphere: "jelly sandwich" or "crème brûlée"? *GSA Today* 16, 4.
- Cai, C., Qiu, N., Li, H., Stockli, D.F., Chang, J., Liu, N., 2020. Study of the closure temperature of (U-Th)/He in detrital zircon obtained from natural evolution samples. *Sci. China Earth Sci.* 63 (3), 412–424.
- Calzia, J.P., Rämö, O.T., Jachens, R., Smith, E., Knott, J., 2016. Geology of Shoshone Pluton, Greenwater Range, Southern Death Valley, California 226–237 in *Field Guide for the Death Valley Natural History Conference, 2013*. USGS Open File Report (2016–1064).
- Carrillo, E., Mora, A., Ketcham, R.A., Amorocho, R., Parra, M., Costantino, D., Robles, W., Avellaneda, W., Carvajal, J.S., Corcione, M.F., 2016. Movement vectors and deformation mechanisms in kinematic restorations: A case study from the Colombian Eastern Cordillera. *Interpretation* 4 (1), T31–T48.
- Casey, M., 1980. Mechanics of shear zones in isotropic dilatant materials. *J. Struct. Geol.* 2 (1–2), 143–147.
- Cemen, I., Wright, L.A., 1990. Effect of Cenozoic extension on Mesozoic thrust surfaces. In: *Basin and Range Extensional Tectonics Near the Latitude of Las Vegas, Nevada*, 176, p. 305.
- Cemen, I., Wright, L.A., Drake, R.E., Johnson, F.C., 1985. Cenozoic Sedimentation and Sequence of Deformational Events at the Southeastern End of the Furnace Creek Strike-Slip Fault Zone, Death Valley Region, California (K. T. Biddle & N. Christie-Blick, Eds.): *Strike-Slip Deformation, Basin Formation, and Sedimentation*, 37, pp. 129–141.
- Cemen, I., Wright, L.A., Prave, A.R., Troxel, B.W., 1999. Stratigraphy and tectonic implications of the latest Oligocene and early Miocene sedimentary succession, southernmost Funeral Mountains, Death Valley region, California. In: *Cenozoic Basins of the Death Valley Region*. Special Papers-Geological Society of America, pp. 65–86.
- Chamberlin, R.T., 1910. The Appalachian folds of Central Pennsylvania. *J. Geol.* 18, 228–251.
- Chapman, J.B., Carrapa, B., Ballato, P., DeCelles, P.G., Worthington, J., Oimahmadov, I., Gadoev, M., Ketcham, R., 2017. Intracontinental subduction beneath the Pamir Mountains: Constraints from thermokinematic modeling of shortening in the Tajik fold-and-thrust belt. *GSA Bull.* 1–22. <https://doi.org/10.1130/B31730.1>.
- Chapman, J.B., Greig, R., Haxel, G.B., 2019. Geochemical evidence for an orogenic plateau in the southern U.S. and northern Mexican Cordillera during the Laramide orogeny. *Geology* 1–5. <https://doi.org/10.1130/G47117.1>.
- Chatzaras, V., Tikoff, B., Newman, J., Withers, A.C., Drury, M.R., 2015. Mantle strength of the San Andreas fault system and the role of mantle-crust feedbacks. *Geology* 43, 891–894.
- Chenin, P., Schmalholz, S.M., Manatschal, G., Duret, T., 2020. Impact of crust–mantle mechanical coupling on the topographic and thermal evolutions during the necking phase of 'magma-poor' and 'sediment-starved' rift systems: a numerical modeling study. *Tectonophysics* 228472.
- Clerc, C., Jolivet, L., Ringenbach, J.-C., 2015. Ductile extensional shear zones in the lower crust of a passive margin. *Earth Planet. Sci. Lett.* 431, 1–7. <https://doi.org/10.1016/j.epsl.2015.08.038>.
- Colletini, C., 2011. The mechanical paradox of low-angle normal faults: current understanding and open questions. *Tectonophysics* 510, 253–268. <https://doi.org/10.1016/j.tecto.2011.07.015>.
- Colletini, C., Sibson, R.H., 2001. Normal faults, normal friction? *Geology* 29, 927–930.
- Colletini, C., Tesi, T., Scuderi, M.M., Carpenter, B.M., Viti, C., 2019. Beyond Byerlee friction, weak faults and implications for slip behavior. *Earth Planet. Sci. Lett.* 519, 245–263. <https://doi.org/10.1016/j.epsl.2019.05.011>.
- Coney, P.J., Harms, T.A., 1984. Cordilleran metamorphic core complexes: Cenozoic extensional relics of Mesozoic compression. *Geology* 12 (9), 550. [https://doi.org/10.1130/0091-7613\(1984\)12<550:cmccc>2.0.co;2](https://doi.org/10.1130/0091-7613(1984)12<550:cmccc>2.0.co;2).
- Cooper, F.J., Platt, J.P., Platzman, E.S., Grove, M.J., Seward, G., 2010. Opposing shear senses in a subdetachment mylonite zone: Implications for core complex mechanics. *Tectonics* 29 (4). <https://doi.org/10.1029/2009TC002632> n/a–n/a.
- Cooper, F.J., Platt, J.P., Behr, W.M., 2017. Rheological transitions in the middle crust: insights from Cordilleran metamorphic core complexes. *Solid Earth* 8, 199–215. <https://doi.org/10.5194/se-8-199-2017>.
- Cummins, P.R., Pranantyo, I.R., Pownall, J.M., Griffin, J.D., Meilano, I., Zhao, S., 2020. Earthquakes and tsunamis caused by low-angle normal faulting in the Banda Sea, Indonesia. *Nat. Geosci.* 13 (4), 312–318.
- Dahlstrom, C., 1969. Balanced cross sections. *Can. J. Earth Sci.* 6, 743–757.
- Davis, G.A., Lister, G.S., 1988. Detachment faulting in continental extension; Perspectives from the Southwestern U.S. Cordillera. In: *Processes in Continental Lithospheric Deformation*, Geological Society of America Special Papers. Geological Society of America, pp. 133–160. <https://doi.org/10.1130/SPE218-p133>.
- Deng, H., Ren, J., Pang, X., Rey, P.F., McClay, K.R., Watkinson, I.M., Zheng, J., Luo, P., 2020. South China Sea documents the transition from wide continental rift to continental break up. *Nat. Commun.* 11, 1–9.
- Dickinson, W.R., 2002. The Basin and Range Province as a composite extensional domain. *Int. Geol. Rev.* 44 (1), 1–38.
- Dixon, T.H., Xie, S., 2018. A kinematic model for the evolution of the Eastern California Shear Zone and Garlock Fault, Mojave Desert, California. *Earth Planet. Sci. Lett.* 494, 60–68. <https://doi.org/10.1016/j.epsl.2018.04.050>.
- Eppelbaum, L., Kutasov, I., Pilchin, A., 2014. *Applied Geothermics*. Springer Science & Business.
- Faulkner, D.R., Mitchell, T.M., Healy, D., Heap, M.J., 2006. Slip on "weak" faults by the rotation of regional stress in the fracture damage zone. *Nat. Publ. Group* 444 (7121), 922–925.
- Fitzgerald, P.G., Duebendorfer, E.M., Faults, J.E., O'Sullivan, P., 2009. South Virgin-White Hills detachment fault system of SE Nevada and NW Arizona: Applying apatite fission track thermochronology to constrain the tectonic evolution of a major continental detachment fault. *Tectonics* 28 (2). <https://doi.org/10.1029/2007TC002194> n/a–n/a.
- Fox, M., Carter, A., 2020. Heated topics in Thermochronology and paths towards resolution. *Geosciences* 10, 375.
- Freed, A.M., Bürgmann, R., Herring, T., 2007. Far-reaching transient motions after Mojave earthquakes require broad mantle flow beneath a strong crust. *Geophys. Res. Lett.* 34 (19).
- Fridrich, C.J., Thompson, R.A., 2011. Cenozoic Tectonic Reorganizations of the Death Valley Region, Southeast California and Southwest Nevada: United States Geological Survey Paper.
- Fridrich, C.J., Thompson, R.A., Slate, J.L., Berry, M.E., Machette, M.N., 2012. Geologic map of the southern Funeral Mountains including nearby groundwater discharge sites in Death Valley National Park, California and Nevada. *Sci. Investig. Map*. <https://doi.org/10.3133/sim3151>.
- Giallorenzo, M.A., Wells, M.L., Yonkee, W.A., Stockli, D.F., Wernicke, B.P., 2018. Timing of exhumation, Wheeler Pass thrust sheet, southern Nevada and California: late Jurassic to middle cretaceous evolution of the southern Sevier fold-and-thrust belt. *GSA Bull.* 130, 558–579. <https://doi.org/10.1130/B31777.1>.
- Gilbert, H., 2012. Crustal structure and signatures of recent tectonism as influenced by ancient terranes in the western United States. *Geosphere* 8 (1), 141–157.
- Groshong, R.H., 1994. Area balance, depth to detachment, and strain in extension. *Tectonics* 13, 1488–1497. <https://doi.org/10.1029/94tc02020>.
- Groshong, R.H., 1996. Construction and validation of extensional cross sections using lost area and strain, with application to the Rhine Graben. *Geol. Soc. Lond., Spec. Publ.* 99, 79–87.
- Groshong Jr., R.H., Bond, C., Gibbs, A., Ratliff, R., Wiltchko, D.V., 2012. Preface: Structural balancing at the start of the 21st century: 100 years since Chamberlin. *J. Struct. Geol.* 41, 1–5. <https://doi.org/10.1016/j.jsg.2012.03.010>.
- Grujic, D., 2006. Channel flow and continental collision tectonics: an overview. *Geol. Soc. Lond., Spec. Publ.* 268, 25–37.
- Gueydan, F., Précigout, J., 2014. Modes of continental rifting as a function of ductile strain localization in the lithospheric mantle. *Tectonophysics* 612–613 (C), 18–25. <https://doi.org/10.1016/j.tecto.2013.11.029>.
- Gueydan, F., Morency, C., Brun, J.-P., 2008. Continental rifting as a function of lithosphere mantle strength. *Tectonophysics* 460 (1–4), 83–93. <https://doi.org/10.1016/j.tecto.2008.08.012>.
- Gueydan, F., Précigout, J., Montési, L.G.J., 2014. Strain weakening enables continental plate tectonics. *Tectonophysics* 631 (C), 189–196. <https://doi.org/10.1016/j.tecto.2014.02.005>.
- Haines, S.H., van der Pluijm, B.A., 2008. Clay quantification and Ar–Ar dating of synthetic and natural gouge: application to the Miocene Sierra Mazatán detachment fault, Sonora, Mexico. *J. Struct. Geol.* 30 (4), 525–538.
- Haines, S.H., van der Pluijm, B.A., 2012. Patterns of mineral transformations in clay gouge, with examples from low-angle normal fault rocks in the western USA. *J. Struct. Geol.* 43, 2–32. <https://doi.org/10.1016/j.jsg.2012.05.004>.
- Haines, S.H., van der Pluijm, B.A., Ikari, M.J., Saffer, D.M., Marone, C., 2009. Clay fabric intensity in natural and artificial fault gouges: Implications for brittle fault zone processes and sedimentary basin clay fabric evolution. *J. Geophys. Res. Solid Earth* 114 (B5).
- Harry, D.L., Sawyer, D.S., Leeman, W.P., 1993. The mechanics of continental extension in western North America: Implications for the magmatic and structural evolution of the Great Basin. *Earth Planet. Sci. Lett.* 117, 59–71.
- Hartog Den, S.A.M., Spiers, C.J., 2013. Influence of subduction zone conditions and gouge composition on frictional slip stability of megathrust faults. *Tectonophysics* 600, 75–90. <https://doi.org/10.1016/j.tecto.2012.11.006>.
- Hartog Den, S.A.M., Peach, C.J., de Winter, D.A.M., Spiers, C.J., Shimamoto, T., 2012. Frictional properties of megathrust fault gouges at low sliding velocities: New data on effects of normal stress and temperature. *J. Struct. Geol.* 38, 156–171. <https://doi.org/10.1016/j.jsg.2011.12.001>.
- Hartog Den, S.A.M., Niemeijer, A.R., Spiers, C.J., 2013. Friction on subduction megathrust faults: beyond the illite–muscovite transition. *Earth Planet. Sci. Lett.* 373, 8–19. <https://doi.org/10.1016/j.epsl.2013.04.036>.
- Healy, D., 2009. Anisotropy, pore fluid pressure and low angle normal faults. *J. Struct. Geol.* 31 (6), 561–574. <https://doi.org/10.1016/j.jsg.2009.03.001>.
- Helfrich, A.L., Buford Parks, V.M., Thigpen, J.R., McQuarrie, N., 2020. Testing interpretations of the displacement magnitude of the Teton fault and uplift of the Teton Range, WY with integrated flexural-kinematic and thermal modeling. *Geol. Soc. Am. Abstr. Programs* 52 (6). <https://doi.org/10.1130/abs/2020AM-356016>.

- Hirth, G., Teysier, C., Dunlap, J.W., 2001. An evaluation of quartzite flow laws based on comparisons between experimentally and naturally deformed rocks. *Int. J. Earth Sci. (Geol Rundsch)* 90, 77–87. <https://doi.org/10.1007/s005310000152>.
- Hoisch, T.D., Simpson, C., 1993. Rise and tilt of metamorphic rocks in the lower plate of a detachment fault in the Funeral Mountains, Death Valley, California. *J. Geophys. Res.* 98, 6805–6827. <https://doi.org/10.1029/92jb02411>.
- Hoisch, T.D., Heizler, M.T., Zartman, R.E., 1997. Timing of detachment faulting in the Bullfrog Hills and Bare Mountain area, Southwest Nevada: Inferences from ⁴⁰Ar/³⁹Ar, K-Ar, U-Pb, and fission track thermochronology. *J. Geophys. Res.* 102, 2815–2833. <https://doi.org/10.1029/96jb03220>.
- Holm, D.K., 1995. Relation of deformation and multiple intrusion in the Death Valley extended region, California, with implications for magma entrapment mechanism. *J. Geophys. Res.* 100, 10495–10505. <https://doi.org/10.1029/94jb03255>.
- Holm, D.K., Dokka, R.K., 1991. Major late Miocene cooling of the middle crust associated with extensional orogenesis in the Funeral Mountains. *California* 18, 1775–1778. <https://doi.org/10.1029/91gl02079>.
- Holm, D.K., Dokka, R.K., 1993. Interpretation and tectonic implications of cooling histories: an example from the Black Mountains, Death Valley extended terrane, California. *Earth Planet. Sci. Lett.* 116, 63–80. [https://doi.org/10.1016/0012-821X\(93\)90045-B](https://doi.org/10.1016/0012-821X(93)90045-B).
- Holm, D.K., Snow, J.K., Lux, D.R., 1992. Thermal and barometric constraints on the intrusive and unroofing history of the Black Mountains: Implications for timing, initial dip, and kinematics of detachment faulting in the Death Valley Region, California. *Tectonics* 11 (3), 507–522. <https://doi.org/10.1029/92tc00211>.
- Hughes, C.A., Jessup, M.J., Shaw, C.A., Newell, D.L., 2019. Deformation conditions during syn-convergent extension along the Cordillera Blanca shear zone, Peru. *Geosphere* 1–26. <https://doi.org/10.1130/GES02040.1>.
- Huismans, R., Beaumont, C., 2011. Depth-dependent extension, two-stage breakup and cratonic underplating at rifted margins. *Nature* 473, 74–78. <https://doi.org/10.1038/nature09988>.
- Hussein, M., Serpa, L., Doser, D., Velasco, A., 2011. Imaging the deep structure of the Central Death Valley basin using receiver function, gravity, and magnetic data. *Int. J. Geosci.* 2 (04), 676.
- Jackson, J.A., 2002. Strength of the continental lithosphere: time to abandon the jelly sandwich? *GSA Today* 12, 4–10.
- Jackson, J.A., White, N.J., 1989. Normal faulting in the upper continental crust: observations from regions of active extension. *J. Struct. Geol.* 11, 15–36. [https://doi.org/10.1016/0191-8141\(89\)90033-3](https://doi.org/10.1016/0191-8141(89)90033-3).
- Jaupart, C., Mareschal, J.-C., Iarotsky, L., 2016. Radiogenic heat production in the continental crust. *Lithos* 262, 398–427. <https://doi.org/10.1016/j.lithos.2016.07.017>.
- Johnstone, S.A., Colgan, J.P., 2018. Interpretation of low-temperature thermochronometer ages from tilted normal fault blocks. *Tectonics* 37, 3647–3667. <https://doi.org/10.1029/2018TC0005207>.
- Jolivet, L., Menant, A., Clerc, C., Sternai, Pietro, Bellahsen, N., Leroy, S., Pik, R., Stab, M., Facenna, C., Gorini, C., 2018. Extensional crustal tectonics and crust-mantle coupling, a view from the geological record. *Earth Sci. Rev.* 185, 1187–1209. <https://doi.org/10.1016/j.earscirev.2018.09.010>.
- Ketcham, R.A., 1996. Thermal models of core-complex evolution in Arizona and New Guinea: Implications for ancient cooling paths and present-day heat flow. *Tectonics* 15, 933–951. <https://doi.org/10.1029/96tc00033>.
- Korchinski, M., Rey, P.F., Mondy, L., Teysier, C., Whitney, D.L., 2018. Numerical investigation of deep-crust behavior under lithospheric extension. *Tectonophysics* 726, 137–146. <https://doi.org/10.1016/j.tecto.2017.12.029>.
- Kruse, S., McNutt, M., Phipps-Morgan, J., Royden, L., Wernicke, B.P., 1991. Lithospheric extension near Lake Mead, Nevada: a model for ductile flow in the lower crust. *J. Geophys. Res.* 96, 4435–4456. <https://doi.org/10.1029/90jb02621>.
- Labotka, T.C., 1980. Petrology of a medium-pressure regional metamorphic terrane, Funeral Mountains, California. *Rocky Mt. Geol.* 65, 670–689.
- Labrousse, L., Huet, B., Le Pourhiet, L., Jolivet, L., Burrov, E., 2016. Rheological implications of extensional detachments: Mediterranean and numerical insights. *Earth Sci. Rev.* 161, 233–258. <https://doi.org/10.1016/j.earscirev.2016.09.003>.
- Lavier, L.L., Manatschal, G., 2006. A mechanism to thin the continental lithosphere at magma-poor margins. *Nature* 440, 324–328. <https://doi.org/10.1038/nature04608>.
- Lechler, A.R., Niemi, N.A., Hren, M.T., Lohmann, K.C., 2013. Paleoelevation estimates for the northern and central proto-Basin and Range from carbonate clumped isotope thermometry. *Tectonics* 32 (3), 295–316. <https://doi.org/10.1002/tect.20016>.
- Lee, E.J., Chen, P., Jordan, T.H., Maechling, P.B., Denolle, M.A., Beroza, G.C., 2014. Full-3-D tomography for crustal structure in southern California based on the scattering-integral and the adjoint-wavefield methods. *J. Geophys. Res. Solid Earth* 119 (8), 6421–6451.
- Lister, G.S., Etheridge, M.A., Symonds, P.A., 1986. Detachment faulting and the evolution of passive continental margins. *Geology* 14, 246. [https://doi.org/10.1130/0091-7613\(1986\)14<246:dfateo>2.0.co;2](https://doi.org/10.1130/0091-7613(1986)14<246:dfateo>2.0.co;2).
- Lister, G.S., Etheridge, M.A., Symonds, P.A., 1991. Detachment models for the formation of passive continental margins. *Tectonics* 10, 1038–1064. <https://doi.org/10.1029/90tc01007>.
- Liu, Shaozhuo, Shen, Z.-K., Bürgmann, R., Jónsson, S., 2021. Thin crème brûlée rheological structure for the Eastern California Shear Zone. *Geology*. 49 (2), 216–221.
- Long, S.P., Walker, J.P., 2015. Geometry and kinematics of the Grant Range brittle detachment system, eastern Nevada, USA: an end-member style of upper crustal extension. *Tectonics* 34, 1837–1862.
- Luckow, H., Pavlis, T., Serpa, L., Guest, B., Wagner, D., Snee, L., Hensley, T., Korjenkov, A., 2005. Late Cenozoic sedimentation and volcanism during transtensional deformation in Wingate Wash and the Owlhead Mountains, Death Valley. *Earth Sci. Rev.* 73, 177–219. <https://doi.org/10.1016/j.earscirev.2005.07.013>.
- Lutz, B.M., Axen, G.J., Wells, M.L., Ketcham, R.A., 2019. Crustal-scale mechanical heterogeneity along a low-angle normal fault: Funeral Mountains, California. *AGUFM* 2019, T32A–02.
- Mattinson, C.G., Colgan, J.P., Metcalf, J.R., Miller, E.L., Wooden, J.L., 2007. Late Cretaceous to Paleocene metamorphism and magmatism in the Funeral Mountains metamorphic core complex, Death Valley, California. In: *Special Paper 419: Convergent Margin Terranes and Associated Regions: A Tribute to W.G. Ernst*, Geological Society of America, pp. 205–223.
- McKenzie, D., Nimmo, F., Jackson, J.A., Gans, P.B., Miller, E.L., 2000. Characteristics and consequences of flow in the lower crust. *J. Geophys. Res. Solid Earth* 105 (B5), 11029–11046. <https://doi.org/10.1029/1999jb900446>.
- McQuarrie, N., Ehlers, T.A., 2015. Influence of thrust belt geometry and shortening rate on thermochronometer cooling ages: Insights from the thermokinematic and erosion modeling of the Bhutan Himalaya. *Tectonics* 34, 1055–1079. <https://doi.org/10.1002/2014tc003783>.
- McQuarrie, N., Ehlers, T.A., 2017. Techniques for understanding fold-and-thrust belt kinematics and thermal evolution. In: *Linkages and Feedbacks in Orogenic Systems*. Geological Society of America, pp. 1–30. [https://doi.org/10.1130/2017.1213\(02\)](https://doi.org/10.1130/2017.1213(02)).
- McQuarrie, N., Wernicke, B.P., 2005. An animated tectonic reconstruction of southwestern North America since 36 Ma. *Geosphere* 1 (3), 147–172.
- Melosh, H.J., 1990. Mechanical basis for low-angle normal faulting in the Basin and Range province. *Nature* 343 (6), 331–335. <https://doi.org/10.1038/343331a0>.
- Mizera, M., Little, T., Boulton, C., Prior, D., Watson, E., Biemiller, J., White, J., Shigematsu, N., 2020. Slow-to-Fast deformation in Mafic Fault rocks on an active low-angle normal fault, Woodlark Rift, SE Papua New Guinea. *Geochem. Geophys. Geosyst.* (doi: e2020GC009171).
- Mohn, G., Manatschal, G., Beltrando, M., Masini, E., Kuznir, N., 2012. Necking of continental crust in magma-poor rifted margins: Evidence from the fossil Alpine Tethys margins. *Tectonics* 31 (1).
- Monastero, F.C., Walker, J.D., Katzenstein, A.M., Sabin, A.E., 2002. Neogene evolution of the Indian Wells Valley, East-Central California. *Geol. Soc. Am. Mem.* 195, 199–228.
- Monigle, P.W., Nabelek, J., Braunmiller, J., Carpenter, N.S., 2012. Evidence for low-angle normal faulting in the Pumqu-Xianza Rift, Tibet. *Geophys. J. Int.* 190, 1335–1340. <https://doi.org/10.1111/j.1365-246X.2012.05581.x>.
- Mora, A., Casallas, W., Ketcham, R.A., Gomez, D., Parra, M., Namson, J., Stocklie, D., Almendral, A., Robles, W., Ghorbal, B., 2015. Kinematic restoration of contractional basement structures using thermokinematic models: a key tool for petroleum system modeling. *APPG Bull.* 99, 1575–1598. <https://doi.org/10.1306/04281411108>.
- Naliboff, J., Buitter, S.J.H., 2015. Rift reactivation and migration during multiphase extension. *Earth Planet. Sci. Lett.* 421, 58–67. <https://doi.org/10.1016/j.epsl.2015.03.050>.
- Naliboff, J.B., Buitter, S.J.H., Péron-Pinvidic, G., Osmundsen, P.T., Tetreault, J., 2017. Complex fault interaction controls continental rifting. *Nat. Commun.* 8, 25. <https://doi.org/10.1038/s41467-017-00904-x>.
- Niemi, N., 2012. Geologic map of the Central Grapevine Mountains, Inyo County, California, and Esmeralda and Nye Counties, Nevada. *Geol. Soc. Am.* <https://doi.org/10.1130/2012.DMCH012>.
- Oldow, J.S., Kohler, G., Donelick, R.A., 1994. Late Cenozoic extensional transfer in the Walker Lane strike-slip belt, Nevada. *Geology* 22, 637. [https://doi.org/10.1130/0091-7613\(1994\)022<0637:lccitit>2.3.co;2](https://doi.org/10.1130/0091-7613(1994)022<0637:lccitit>2.3.co;2).
- Oner, Z., Dilek, Y., 2013. Fault kinematics in supradetachment basin formation, Menderes core complex of western Turkey. *Tectonophysics* 608, 1394–1412.
- Osmundsen, P.T., Péron-Pinvidic, G., 2018. Crustal-scale fault interaction at rifted margins and the formation of domain-bounding breakaway complexes: insights from offshore Norway. *Tectonics* 9, 1027–1030. <https://doi.org/10.1002/2017TC004792>.
- Pang, G., Koper, K.D., Mesimeri, M., Pankow, K.L., Baker, B., Farrell, J., Holt, J., Hale, J.M., Roberson, P., Burlacu, R., 2020. Seismic analysis of the 2020 Magna, Utah, earthquake sequence: Evidence for a listric Wasatch fault. *Geophys. Res. Lett.* 47 (e2020GL089798).
- Pérez-Gussinyé, M., Reston, T.J., 2001. Rheological evolution during extension at nonvolcanic rifted margins: Onset of serpentinization and development of detachments leading to continental breakup. *J. Geophys. Res. Solid Earth* 106 (B3), 3961–3975.
- Péron-Pinvidic, G., Manatschal, G., 2009. The final rifting evolution at deep magma-poor passive margins from Iberia-Newfoundland: a new point of view. *Int. J. Earth Sci. (Geol Rundsch)* 98, 1581–1597.
- Péron-Pinvidic, G., Manatschal, G., Osmundsen, P.T., 2013. Structural comparison of archetypal Atlantic rifted margins: a review of observations and concepts. *Mar. Pet. Geol.* 43, 21–47. <https://doi.org/10.1016/j.marpetgeo.2013.02.002>.
- Pinet, C., Jaupart, C., 1987. The vertical distribution of radiogenic heat production in the Precambrian crust of Norway and Sweden: geothermal implications. *Geophys. Res. Lett.* 14, 260–263.
- Platt, J.P., Behr, W.M., 2011. Lithospheric shear zones as constant stress experiments. *Geology* 39 (2), 127–130. <https://doi.org/10.1130/G31561.1>.
- Platt, J.P., Behr, W.M., Cooper, F.J., 2015. Metamorphic core complexes: windows into the mechanics and rheology of the crust. *J. Geol. Soc.* 172 (1), 9–27. <https://doi.org/10.1144/jgs2014-036>.
- Rak, A.J., McQuarrie, N., Ehlers, T.A., 2017. Kinematics, exhumation, and sedimentation of the North Central Andes (Bolivia): an integrated thermochronometer and thermokinematic modeling approach. *Tectonics* 36, 2524–2554. <https://doi.org/10.1002/2016TC004440>.
- Reiners, P.W., 2005. Zircon (U-Th)/he thermochronometry. *Rev. Mineral. Geochem.* 58, 151–179.

- Reston, T.J., 1990a. Shear in the lower crust during extension: not so pure and simple. *Tectonophysics* 173 (1–4), 175–183.
- Reston, T.J., 2009a. The structure, evolution and symmetry of the magma-poor rifted margins of the North and Central Atlantic: A synthesis. *Tectonophysics* 468 (1–4), 6–27.
- Reston, T.J., 1990b. The lower crust and the extension of the continental lithosphere: kinematic analysis of BIRPS deep seismic data. *Tectonics* 9 (5), 1235–1248.
- Reston, T.J., McDermott, K.G., 2011. Successive detachment faults and mantle unroofing at magma-poor rifted margins. *Geology* 39 (11), 1071–1074.
- Rey, P., Vanderhaeghe, O., Teyssier, C., 2001. Gravitational collapse of the continental crust: definition, regimes and modes. *Tectonophysics* 342 (3–4), 435–449. [https://doi.org/10.1016/S0040-1951\(01\)00174-3](https://doi.org/10.1016/S0040-1951(01)00174-3).
- Rey, P.F., Teyssier, C., Whitney, D.L., 2009a. The role of partial melting and extensional strain rates in the development of metamorphic core complexes. *Tectonophysics* 477 (3–4), 135–144. <https://doi.org/10.1016/j.tecto.2009.03.010>.
- Rey, P.F., Teyssier, C., Whitney, D.L., 2009b. Extension rates, crustal melting, and core complex dynamics. *Geology* 37 (5), 391–394. <https://doi.org/10.1130/G25460A.1>.
- Robinson, A.C., Yin, A., Lovera, O.M., 2010. The role of footwall deformation and denudation in controlling cooling age patterns of detachment systems: an application to the Kongur Shan extensional system in the Eastern Pamir, China. *Tectonophysics* 496, 28–43. <https://doi.org/10.1016/j.tecto.2010.10.003>.
- Rowe, C.D., Griffith, W.A., 2015. Do faults preserve a record of seismic slip: A second opinion. *J. Struct. Geol.* 78 (C), 1–26. <https://doi.org/10.1016/j.jsg.2015.06.006>.
- Sass, J.H., Lachenbruch, A.H., Galanis Jr., S.P., Morgan, P., Priest, S.S., Moses Jr., T.H., Munroe, R.J., 2008. Thermal regime of the southern Basin and Range Province and Nevada. *J. Geophys. Res.* 99, 22093–22119. <https://doi.org/10.1029/94JB01891>.
- Sauer, K.M., Wells, M.L., Hoisch, T.D., 2013. Significance of orthogonal flow in the Funeral Mountains metamorphic core complex, Death Valley, California: Insights from geochronology and microstructural analysis. *AGUFM* 2013, T53C–2600.
- Sawyer, D.A., Fleck, R.J., Lanphere, M.A., Warren, R.G., Broxton, D.E., Hudson, M.R., 1994. Episodic caldera volcanism in the Miocene southwestern Nevada volcanic field: revised stratigraphic framework, ⁴⁰Ar/³⁹Ar geochronology, and implications for magmatism and extension. *Geol. Soc. Am. Bull.* 106, 1304–1318. [https://doi.org/10.1130/0016-7606\(1994\)106<1304:ecvitm>2.3.co;2](https://doi.org/10.1130/0016-7606(1994)106<1304:ecvitm>2.3.co;2).
- Scholz, C.H., 2002. *The Mechanics of Earthquakes and Faulting*. Cambridge University Press.
- Schutt, D.L., Lowry, A.R., Buehler, J.S., 2018. Moho temperature and mobility of lower crust in the western United States. *Geology* 46, 219–222. <https://doi.org/10.1130/G39507.1>.
- Selverstone, J., Axen, G.J., Luther, A., 2012. Fault localization controlled by fluid infiltration into mylonites: Formation and strength of low-angle normal faults in the midcrustal brittle-plastic transition. *J. Geophys. Res.* 117. <https://doi.org/10.1029/2012JB009171> n/a–n/a.
- Singleton, J.S., 2015. The transition from large-magnitude extension to distributed dextral faulting in the Buckskin-Rawhide metamorphic core complex, west-central Arizona. *Tectonics* 34 (8), 1685–1708.
- Singleton, J.S., Mosher, S., 2012. Mylonitization in the lower plate of the Buckskin-Rawhide detachment fault, west-Central Arizona: Implications for the geometric evolution of metamorphic core complexes. *J. Struct. Geol.* 39, 180–198. <https://doi.org/10.1016/j.jsg.2012.02.013>.
- Sizemore, T., Wielicki, M.M., Cemen, I., Stockli, D., Heizler, M., Robinson, D., 2019. Structural evolution of central Death Valley, California, using new thermochronometry of the Badwater turtleback. *Lithosphere*.
- Snow, J.K., Wernicke, B.P., 2000. Cenozoic tectonism in the central Basin and Range; magnitude, rate, and distribution of upper crustal strain. *Am. J. Sci.* 300, 659–719. <https://doi.org/10.2475/ajs.300.9.659>.
- Snow, J.K., Lux, D.R., Wright, L.A., Troxel, B.W., 1999. Tectono-Sequence Stratigraphy of Tertiary Rocks in the Cottonwood Mountains and Northern Death Valley Area, California and Nevada: Cenozoic basins of the Death Valley region: Geological Society of America Special Paper, 333, pp. 17–64.
- Spencer, J.E., 1984. Role of tectonic denudation in warping and uplift of low-angle normal faults. *Geology* 12, 95. [https://doi.org/10.1130/0091-7613\(1984\)12<95:rotdiv>2.0.co;2](https://doi.org/10.1130/0091-7613(1984)12<95:rotdiv>2.0.co;2).
- Spencer, J.E., Chase, C.G., 1989. Role of crustal flexure in initiation of low-angle normal faults and implications for structural evolution of the basin and range province. *J. Geophys. Res.* 94 (B2), 1765. <https://doi.org/10.1029/jb094ib02p01765>.
- Stipp, M., StuEinitz, H., Heilbronner, R., Schmid, S.M., 2002. The eastern Tonalite fault zone: a “natural laboratory” for crystal plastic deformation of quartz over a temperature range from 250 to 700 C. *J. Struct. Geol.* 24, 1861–1884.
- Stockli, D.F., 2005. Application of low-temperature thermochronometry to extensional tectonic settings. *Rev. Mineral. Geochem.* 58 (1), 411–448. <https://doi.org/10.2138/rmg.2005.58.16>.
- Stockli, D.F., Dumitru, T.A., McWilliams, M.O., Farley, K.A., 2003. Cenozoic tectonic evolution of the White Mountains, California and Nevada. *Geol. Soc. Am. Bull.* 115, 788–816. [https://doi.org/10.1130/0016-7606\(2003\)115<0788:ctetw>2.0.co;2](https://doi.org/10.1130/0016-7606(2003)115<0788:ctetw>2.0.co;2).
- Styron, R.H., Hetland, E.A., 2014. Estimated likelihood of observing a large earthquake on a continental low-angle normal fault and implications for low-angle normal fault activity. *Geophys. Res. Lett.* 41, 2342–2350. <https://doi.org/10.1002/2014GL059335>.
- Suppe, J., 1985. *Principles of Structural Geology* (Prentice Hall).
- Thacker, J.O., Karlstrom, K.E., Crossey, L.J., Crow, R.S., Cassidy, C.E., Beard, L.S., Singleton, J.S., Strickland, E.D., Seymour, N.M., Wyatt, M.R., 2020. Post–12 Ma deformation in the lower Colorado River corridor, southwestern USA: Implications for diffuse transension and the Bouse Formation. *Geosphere* 16 (1), 111–135.
- Tokle, L., Hirth, G., Behr, W.M., 2019. Flow laws and fabric transitions in wet quartzite. *Earth Planet. Sci. Lett.* 505, 152–161. <https://doi.org/10.1016/j.epsl.2018.10.017>.
- Treagus, S.H., 1973. Buckling stability of a viscous single-layer system, oblique to the principal compression. *Tectonophysics* 19, 271–289.
- van der Pluijm, B.A., Hall, C.M., Vrolijk, P.J., Pevear, D.R., Covey, M.C., 2001. The dating of shallow faults in the Earth’s crust. *Nat. Publ. Group* 412 (6843), 172–175.
- Walker, J.D., Bidgoli, T.S., Didericksen, B.D., Stockli, D.F., Andrew, J.E., 2014. Middle Miocene to recent exhumation of the Slate Range, eastern California, and implications for the timing of extension and the transition to transension. *Geosphere* 10, 276–291. <https://doi.org/10.1130/ges00947.1>.
- Wdowinski, S., Axen, G.J., 1992. Isostatic rebound due to tectonic denudation: a viscous flow model of a layered lithosphere. *Tectonics* 11, 303–315. <https://doi.org/10.1029/91tc02341>.
- Wells, M.L., 2001. Rheological control on the initial geometry of the Raft River detachment fault and shear zone, western United States. *Tectonics* 20, 435–457. <https://doi.org/10.1029/2000TC001202>.
- Wernicke, B.P., 1985. Uniform-sense normal simple shear of the continental lithosphere. *Can. J. Earth Sci.* 22, 108–125. <https://doi.org/10.1139/e85-009>.
- Wernicke, B.P., 1992. Cenozoic extensional tectonics of the U.S. Cordillera. In: *The Geology of North America*, 80301. Geological Society of America, Boulder, Colorado, pp. 553–582. <https://doi.org/10.1130/dnag-gna-g3.553>.
- Wernicke, B.P., 1995. Low-angle normal faults and seismicity: a review. *J. Geophys. Res.* 100, 20159–20174. <https://doi.org/10.1029/95jb01911>.
- Wernicke, B.P., Axen, G.J., 1988. On the role of isostasy in the evolution of normal fault systems. *Geology* 16, 848. [https://doi.org/10.1130/0091-7613\(1988\)016<0848:otroii>2.3.co;2](https://doi.org/10.1130/0091-7613(1988)016<0848:otroii>2.3.co;2).
- Wernicke, B.P., Spencer, J.E., Burchfiel, B.C., Guth, P.L., 1982. Magnitude of crystal extension in the southern Great Basin. *Geology* 10, 499. [https://doi.org/10.1130/0091-7613\(1982\)10<499:moceti>2.0.co;2](https://doi.org/10.1130/0091-7613(1982)10<499:moceti>2.0.co;2).
- Wernicke, B.P., Axen, G.J., Snow, J.K., 1988. Basin and Range extensional tectonics at the latitude of Las Vegas, Nevada. *Geol. Soc. Am. Bull.* 100, 1738–1757. [https://doi.org/10.1130/0016-7606\(1988\)100<1738:bareta>2.3.co;2](https://doi.org/10.1130/0016-7606(1988)100<1738:bareta>2.3.co;2).
- Westaway, R., 1999. *The mechanical feasibility of low-angle normal faulting*. *Tectonophysics* 308, 407–443.
- Whitney, D.L., Teyssier, C., Rey, P., Buck, W.R., 2013. Continental and oceanic core complexes. *GSA Bull.* 125 (3–4), 273–298. <https://doi.org/10.1130/B30754.1>.
- Wijns, C., Weinberg, R., Gessner, K., Moresi, L., 2005. Mode of crustal extension determined by rheological layering. *Earth Planet. Sci. Lett.* 236, 120–134. <https://doi.org/10.1016/j.epsl.2005.05.030>.
- Wolfe, M.R., Stockli, D.F., 2010. Zircon (U–Th)/He thermochronometry in the KTB drill hole, Germany, and its implications for bulk He diffusion kinetics in zircon. *Earth Planet. Sci. Lett.* 295 (1–2), 69–82.
- Workman, J.B., Menges, C., Fridrich, C.J., Thompson, R.A., 2016. *Geologic Map of Death Valley National Park, Nevada and California*. Geosciences and Environmental Change Science Center. Geological Society of America, p. 286651.
- Wright, L.A., Troxel, B.W., 1993. *Geologic map of the central and northern Funeral Mountains and adjacent areas*. In: *Death Valley region, southern California: US Geological Survey Miscellaneous Investigations Series Map I-2305, scale 1*.
- Wust, S.L., 1986. Regional correlation of extension directions in Cordilleran metamorphic core complexes. *Geology* 14 (10), 828. [https://doi.org/10.1130/0091-7613\(1986\)14<828:rcocedi>2.0.co;2](https://doi.org/10.1130/0091-7613(1986)14<828:rcocedi>2.0.co;2).
- Yin, A., 1989. Origin of regional, rooted low-angle normal faults: a mechanical model and its tectonic implications. *Tectonics* 8, 469–482. <https://doi.org/10.1029/tc008i03p00469>.
- Yonkee, W.A., Eleogram, B., Wells, M.L., Stockli, D.F., Kelley, S., Barber, D.E., 2019. Fault slip and exhumation history of the Willard thrust sheet, sevier fold-thrust belt, Utah: relations to Wedge propagation, Hinterland Uplift, and Foreland Basin sedimentation. *Tectonics* 38, 2850–2893. <https://doi.org/10.1029/2018TC005444>.
- Zhou, Q., Liu, L., 2019. Topographic evolution of the western United States since the early Miocene. *Earth Planet. Sci. Lett.* 514, 1–12. <https://doi.org/10.1016/j.epsl.2019.02.029>.
- Zuza, A.V., Cao, W., 2020. Seismogenic thickness of California: Implications for thermal structure and seismic hazard. *Tectonophysics* 228426.
- Zuza, A.V., Cao, W., Hinz, N.H., DesOrmeau, J.W., Odlum, M.L., Stockli, D.F., 2019. Footwall rotation in a regional detachment fault system: evidence for horizontal-axis rotational flow in the Miocene Searchlight pluton, NV. *Tectonics* 38 (7), 2506–2539.